## TITLE

# The *Yersinia pestis* virulence effector YopM binds to a key regulatory site on the human pyrin death domain to inhibit inflammasome activation and effector-triggered immunity

## AUTHORS

Bethany W. Mwaura[1], Adam R. Simard[2], Morgan L. Pettis[1], Ao R. Liu[2], Dean R. Madden[2], James B. Bliska[1]

[1]Department of Microbiology and Immunology and [2]Department of Biochemistry and Cell Biology, Geisel School of Medicine at Dartmouth, Hanover, NH 03755

## CORRESPONDING AUTHOR

James B. Bliska

## PREPRINT SERVER

bioRxiv

## CLASSIFICATION

Microbiology

## KEY WORDS

*Yersinia,* YopM, Pyrin, Inflammasome, Effector-triggered Immunity

## ABSTRACT

Bacteria in the genus *Yersinia* use a type III secretion system to inject effectors into host cells to disrupt multiple signaling processes. Two effectors, YopE and YopT, disrupt host signaling by inactivating RhoA GTPases. Inactivation of RhoA triggers assembly of the pyrin inflammasome in infected phagocytes leading to a protective immune response. A third *Yersinia* effector, YopM, is an essential virulence factor that counteracts YopE- or YopT-triggered immunity by inactivating pyrin. YopM has a leucine-rich repeat (LRR) domain and hijacks the host kinases PRK and RSK to inactivate pyrin by phosphorylation. Previously, the LRR domain of *Yersinia pestis* YopM was implicated in binding to an N-terminal region of human pyrin, which includes the eponymous pyrin domain (PYD), a member of the death domain fold family. In addition, the PYD was shown to be required for phosphorylation of pyrin by YopM. However, the mechanism underlying this interaction is not fully understood. Using a bacterial two-hybrid assay, protein biochemistry and x-ray crystallography, we show that the concave surface of the YopM LRR domain binds to the PYD. We identified critical residues in YopM and the PYD involved in their interaction. Furthermore, we show that YopM codon substitution variants defective for PYD binding fail to inhibit the pyrin inflammasome in human monocytes infected with *Yersinia*. These results give key insights into how *Y. pestis* YopM targets and inhibits the human pyrin inflammasome through binding a key regulatory site on the PYD. In addition, we found that PYD binding is dispensable for YopM to inhibit the murine pyrin inflammasome, suggesting this effector uses a distinct mechanism to target mouse pyrin.

## MAIN TEXT

## INTRODUCTION

Pathogens use a variety of strategies to evade detection and elimination by host immune responses. One method employed by numerous pathogenic bacteria involves injecting effector proteins directly into eukaryotic cells. These effectors can be injected via the type III secretion system (T3SS) which is employed by Gram-negative bacteria that infect both animals and plants (1). The T3SS is a sophisticated protein secretion machinery which spans from the bacterial membrane through the host plasma membrane (2). Human pathogenic species of *Yersinia*, *Shigella* and *Salmonella* among others use a contact-dependent T3SS to secrete effectors, regulate host cell responses and promote pathogenesis (2). Host cells can sense assault by the T3SS and or effectors and mount immune responses (3). In macrophages infected with bacterial pathogens, perturbations induced by T3SSs and/or effectors can result in the assembly of inflammasomes (4). Canonical inflammasomes are multiprotein assemblies that pronmote the recruitment and maturation of caspase-1 into its active form (4). Active caspase-1 cleaves gasdermin-D (GSDMD), pro-IL-18 and pro-IL-1β (5, 6). The N-terminal domain of GSDMD forms pores in the plasma membrane, promoting release of mature IL-18 and IL-1β (5, 6). GSDMD pores can also result in the release of additional pro-inflammatory molecules and intracellular bacteria as a result of cell death, termed pyroptosis (6, 7). Pyroptosis downstream of GSMD pore formation requires plasma membrane rupture mediated by the ninjurin 1 protein (8). To counteract protective immune responses mediated by IL-1β, IL-18 and pyroptosis, virulent bacterial pathogens have evolved the ability to inhibit caspase-1 inflammasomes in host cells (4, 9).

The genus *Yersinia* contains several Gram-negative bacterial pathogens that cause invasive human infections ranging in severity from self-limiting mesenteric lymphadenitis (*Y. pseudotuberculosis*) to lethal plague (*Y. pestis*). *Yersinia* colonize lymphoid tissues and replicate as extracellular microcolonies in phagocyte-rich lesions known as pyogranulonas and a plasmid-encoded T3SS is required for this infection process (10, 11). The T3SS delivers seven effectors named *Yersinia* outer proteins (Yops) into the cytosol of host cells in contact with the bacteria (12). The effectors inhibit key host cell processes, such as proinflammatory cytokine production and phagocytosis (12). YopE and YopT are two *Yersinia* effectors that contribute to the anti-signaling functions of the T3SS by targeting Rho GTPases (13, 14). YopE has a GAP domain that accelerates conversion of GTP to GDP, locking the GTPase in an inactive form (13). YopT is a cysteine protease which cleaves off a C-terminal amino acid and lipid anchor from the GTPase, disrupting its association on host membranes and

108 preventing interaction with downstream targets (14). YopM is a leucine rich repeat (LRR) effector that
109 inhibits the pyrin inflammasome in activated macrophages (15, 16). YopJ is a member of the
110 acetyltransferase effector family (17) that inhibits MAPK and NF-kB signaling pathways to inhibit
111 proinflammatory cytokine production (18, 19). YopJ also cooperates by an unknown mechanism with
112 YopM to inhibit the pyrin inflammasome in activated macrophages (20).
113
114 Inactivation of Rho GTPases (RhoA, -B or -C, hereafter referred to as RhoA) by bacterial toxins or
115 effectors triggers assembly of the pyrin inflammasome by an indirect guard mechanism in phagocytes
116 (21, 22). YopE or YopT triggers assembly of the pyrin inflammasome in activated macrophages
117 infected by *Yersinia* (15, 16, 23, 24). Pyrin, encoded by the Mediterranean fever (*MEFV*) gene, is a
118 cytosolic pattern recognition receptor (PRR) which is preferentially expressed in phagocytes such as
119 macrophages and neutrophils (25, 26). Human pyrin is comprised of the following domains: An N-
120 terminal PYD followed by a linker region, B-box domain, coiled coil domain (CC) and a C-terminal
121 B30.2 domain (Fig. S1A). Murine pyrin is structurally like human pyrin except that it lacks the C
122 terminal B30.2 domain, which is replaced by a short unstructured tail (Fig. S1A) (23, 25, 26). Pyrin is
123 also known as TRIM20 as it belongs to the TRIM family of proteins (27) and forms dimers via the CC
124 domain (Fig. S1B) (28). By analogy to TRIM5 (29), the pyrin B-box potentially mediates the formation
125 of higher order oligomers such as dimers of dimers (30). Pyrin is negatively and positively regulated
126 by multiple mechanisms (21, 23, 30-35). Pyrin is negatively regulated by phosphorylation via the
127 kinase PRK (also known as PKN) which in turn is activated by RhoA. Human pyrin is phosphorylated
128 on serine residues 208 and 242 (205 and 241 on mouse pyrin) on the linker region creating a binding
129 site for 14-3-3 protein dimers (32, 33). Pyrin is also negatively regulated by binding of the PYD to the
130 B-box (31). A model posits that phosphorylated pyrin is rendered inactive as the 14-3-3-bound linker
131 is bent into a hairpin (36) and the PYD is sequestered by the B-box, preventing interaction with ASC
132 (Fig. S1B) (23). In *Yersinia*-infected cells pyrin is activated when YopE or YopT inactivate RhoA, and
133 a positive regulation step leads to dephosphorylation by a phosphoprotein phosphatase (23, 24, 30).
134 According to the model, when pyrin is dephosphorylated, the PYD is released from the B-box and
135 exposed, ASC is recruited, caspase-1 is activated, GSDMD pores are formed and active IL-1β and IL-
136 18 are secreted (23, 30). Pyrin inflammasome activation in phagocytes infected with *Yersinia* is
137 blocked due to the activity of YopM (15, 16). YopM hijacks the host kinases PRK and RSK (37, 38) to
138 phosphorylate pyrin, locking it in an inactive state (15, 23, 39). YopM is crucial for *Yersinia* virulence
139 in mouse models of infection and a *Y. pseudotuberculosis* Δ*yopM* mutant is fully virulent in *Mefv*$^{-/-}$
140 mice, demonstrating that pyrin is the major host target of YopM (16, 40, 41).
141

142 YopM is a member of the bacterial subfamily of leucine rich repeat (LRR) effector proteins (42). (16,
143 40, 41) Pathogenic species and strains of *Yersinia* encode for a variety of different YopM proteins,
144 referred to here as isoforms, with varying numbers of LRRs. Despite these differences in the number
145 and composition of LRRs, all YopM isoforms studied so far have been shown to inhibit the pyrin
146 inflammasome (15, 16). YopM from *Y. pestis* 195/P has been structurally determined and adopts an
147 overall horse-shoe shaped fold comprised of two N-terminal $\alpha$ helices followed by an extended LRR
148 region with short beta strands (43). The two $\alpha$ helices provide a nucleation site that facilitates the
149 folding of the LRRs (43). The N- and C-termini of YopM are unstructured and highly conserved
150 among YopM isoforms. The N-terminus contains the secretion signal required for YopM translocation
151 into host cells (44), and the C-terminal tail is a binding site for the N-terminal kinase domain of host
152 kinase RSK (Fig.S1A) (40, 41, 45).
153
154 During *Yersinia* infection of host phagocytes, YopM acts as a scaffold connecting the host kinases
155 RSK and PRK (37, 38) to allow for pyrin phosphorylation and inactivation (15, 16, 39). Binding to
156 YopM results in autophosphorylation and activation of RSK, which in turn phosphorylates and
157 activates PRK (Fig. S1C) (37). Inflammasome activation was increased when murine macrophages
158 infected with *Y. pseudotuberculosis* were treated with a PRK inhibitor or with siRNAs that reduced
159 expression of *Prk*, suggesting that PRK activity is important for YopM to inhibit pyrin in mouse
160 phagocytes (15). Similarly, inflammasome activation was increased when human monocytes infected
161 with *Y. pestis* were treated with RSK inhibitors or with siRNAs that reduced expression of *Rsk*,
162 suggesting that RSK activity is important for YopM to inhibit pyrin in human phagocytes (39). Park et
163 al. used *in vitro* kinase assays with purified proteins to show that *Y. pestis* YopM could hijack either
164 PRK or RSK to phosphorylate the human pyrin linker, but RSK had much higher activity, and there
165 was no additive effect when both kinases were present (39). These data suggest that both kinases
166 are important, but RSK may be critical for *Y. pestis* YopM to inhibit human pyrin.
167
168 Like other proteins in this family the concave surface of the YopM LRR domain contains exposed
169 amino acid sidechains (43) and is likely important for its scaffolding function in binding host proteins.
170 The kinase domain of PRK binds to YopM (Fig.S1A) (37) and the interaction site appears to be within
171 LRRs 6-15 of the *Y. pestis* isoform (40). Deletion analysis with purified *Y. pestis* YopM variants
172 demonstrated an importance for LRRs 1 and 2 for pyrin binding (39). However, a previous study
173 showed low expression in *Yersinia* of a YopM variant $\Delta$LRR2-3 (41), suggesting that this deletion
174 disrupted YopM stability. Therefore, it's possible that the reduced binding of YopM $\Delta$LRR1-2 to pyrin
175 (39) was a result of structural instability caused by the deletion, and the pyrin binding site on YopM is

176 yet to be established. Additionally, it has been shown that YopM binds to the N-terminus of human
177 pyrin encompassing the PYD and linker (39). Removal of the 90 amino acid PYD prevented
178 phosphorylation of human pyrin by YopM-hijacked RSK in an *in vitro* kinase reaction (39), revealing a
179 key role for this N-terminal domain, but the molecular mechanism underscoring this interaction is not
180 fully understood.
181
182 Here, we provide evidence of direct binding between *Y. pestis* YopM isoforms and the human PYD.
183 We solved a co-crystal structure of YopM bound to human PYD and identify key residues on each
184 involved in their interaction. We also identified YopM variants with alanine substitutions in LRR 5 that
185 are defective for PYD binding *in vitro* and used human monocyte infection assays to demonstrate that
186 PYD binding is critical for YopM to target and inhibit the pyrin inflammasome *in vivo*. Our data also
187 suggest that *Y. pestis* YopM specifically targets the key regulatory Site 2 in the PYD, which has
188 implications for the evolutionary host-pathogen arms race that resulted in FMF and may explain
189 why a distinct mechanism is used to target the mouse pyrin inflammasome.
190
191
192
193 **RESULTS**
194 **YopM Binds to the PYD of Human Pyrin.**
195
196 We tested for direct interactions between *Y. pestis* YopM isoforms and N-terminal domains of human
197 or murine pyrin. We first used the bacterial adenylate cyclase-based two hybrid assay (BACTH) to
198 test for protein-protein interactions. Two different *Y. pestis* YopM isoforms were studied, the 13 LRR
199 version from Pestoides A ($YopM^{PestA}$) and the 15 LRR version from KIM ($YopM^{KIM}$) (46), which have
200 been shown to inhibit the pyrin inflammasome (15, 16). $YopM^{PestA}$ and $YopM^{KIM}$ were expressed as N-
201 terminal fusions with the T25 domain and the human (h) or murine (m) PYD domains as C-terminal
202 fusions to T18. The hPYD and mPYD have 76% identity at the primary sequence level. $YopM^{PestA}$ and
203 $YopM^{KIM}$ showed similar strong binding to hPYD (Fig. 1A, Fig. S2A). Surprisingly, $YopM^{PestA}$ showed
204 no detectable binding to mPYD (Fig. 1B). We further investigated these interactions using GST
205 pulldowns whereby GST-tagged $YopM^{KIM}$ was co-expressed in *Escherichia coli* with His-tagged
206 mPYD or hPYD. Samples of soluble *E. coli* input lysates or pull downs were analyzed by SDS-PAGE
207 and blue staining or anti-His immunoblotting. As compared to the GST alone control, there was low
208 but detectable pull down of mPYD with GST-$YopM^{KIM}$ (Fig. S3). However, as compared to mPYD,
209 there was increased soluble hPYD in the input lysates, and as a result, more hPYD was pulled down
210 with GST-$YopM^{KIM}$ (Fig. S3). Overall, these results suggest that $YopM^{PestA}$ and $YopM^{KIM}$ strongly bind
211 to hPYD, increasing its solubility, and have a lower affinity for mPYD (Fig.S1A).

212

213 Next, we followed up on previous experiments that identified the human pyrin linker as a YopM$^{KIM}$
214 binding site (39). We tested a fragment of the human pyrin linker (amino acids 186-326) which was
215 shown to bind to YopM$^{KIM}$ in GST pull-downs (39). However, we found that this linker fragment
216 (hPyrin186-326) had non-specific binding to GST (Fig. S4A). In addition, we found that YopM$^{KIM}$ did
217 not bind to hPyrin186-326 in BACTH (Fig. S4B). In summary, these results indicate that the PYD is
218 the primary targeting domain for *Y. pestis* YopM isoforms in the human pyrin N-terminal region
219 (Fig.S1A). Since YopM$^{KIM}$ and YopM$^{PestA}$ inhibit mouse pyrin in macrophages and *in vivo* (15, 39),
220 there may be a different mechanism of inflammasome targeting by this effector in murine
221 macrophages, including possible multidentate interactions with the PYD and the linker or other
222 domains.

223

224 **In-Solution State of YopM$^{PestA}$**

225

226 A crystal structure of the 15-LRR YopM protein from *Yersinia pestis* 195/P has been solved (43). In
227 that study, the authors found that YopM$^{195/P}$ formed superhelical tetramers in the crystal lattice. The
228 biological relevance of YopM tetramers is unknown, and it was hypothesized that the tetramers were
229 a crystallographic artifact due to the high levels of calcium in the crystallization conditions (43).
230 However, an analysis of the oligomeric state of YopM in solution was not presented. Other studies
231 have shown that YopM forms higher order oligomers when analyzed by native PAGE in purified form
232 (dimers and tetramers) (41) or in lysates of *Yersinia*-infected macrophages (30, 41), and in the latter
233 case YopM also appeared to interact with dimers and higher order multimers of the host target protein
234 pyrin (30). We ultimately aimed to determine the structure of the smaller 13-LRR YopM$^{PestA}$ isoform in
235 complex with the hPYD but first sought to determine the oligomeric state of YopM$^{PestA}$ in solution. We
236 performed analytical size exclusion chromatography (SEC) of purified full-length YopM$^{PestA}$. We
237 observed that YopM$^{PestA}$ elutes at a faster rate than expected for a monomer on SEC compared to
238 standard proteins, implying that YopM$^{PestA}$ could be a dimer in solution (~90kDa) (Fig. S5A,B),
239 consistent with prior work. Notably, a previous study reported that a 20-LRR YopM from *Y.*
240 *enterocolitica* was a dimer in solution, based on its elution from SEC (47). However, when calibrated
241 against globular standards, SEC retention volume does not accurately predict the molecular mass of
242 non-globular proteins or of proteins which interact with the column matrix (48). Given that YopM is an
243 elongated protein, its migration during SEC is likely unusual compared to the globular protein
244 standards. Therefore, we performed further analysis using SEC coupled with multi-angle light
245 scattering (SEC-MALS) which allows a shape-independent analysis of protein size (48, 49). Data
246 from SEC-MALS indicated that YopM$^{PestA}$ is a monomer (~42kDa) at neutral pH (7.4) in solution (Fig.

247 2A). We further utilized velocity analytical ultracentrifugation (vAUC), another shape-independent
248 method of calculating protein size in solution, to analyze purified YopM$^{PestA}$. vAUC data also
249 suggested that YopM$^{PestA}$ is a monomer in neutral pH (Fig. 2B). Interestingly, the sedimentation
250 coefficient of YopM$^{PestA}$ shifted in low pH (5.0) buffer conditions, consistent with a higher molecular
251 mass (~148 kDa, Fig. 2B). Given that the calculated molecular mass of the trimeric and tetrameric
252 states are ~126 kDa and ~168 kDa, respectively, we cannot unambiguously assign and exact
253 stoichiometry for assembly. However, a tetramer is consistent with previously reported crystal
254 structures (43). Taken together with previous observations, our data suggests that YopM$^{PestA}$ is
255 monomeric at neutral pH, and transitions to an oligomeric form under mildly acidic conditions in
256 solution.
257
258 **Structures of YopM$^{PestA}$-hPYD Complexes**
259
260 Although structural studies of hPYD and closely related YopM isoforms have been conducted in
261 isolation, information pertaining to their complex formation is lacking. Therefore, we sought to
262 determine the structure of a YopM$^{PestA}$-hPYD complex to establish the stereochemical basis for the
263 scaffolding function of YopM. Crystallization trials using the full-length YopM$^{PestA}$ co-purified with
264 hPYD yielded crystals that were difficult to reproduce and optimize (Fig. S6A). Concurrently, a
265 truncation construct of YopM$^{PestA}$ lacking the unstructured first 33 and last 23 residues (43) (amino
266 acids 34-344), was designed to minimize interference with lattice packing by the disordered termini.
267 The resulting protein, henceforth referred to as YopM$^{\Delta N \Delta C}$, has a predicted monomer molecular mass
268 of 35.0 kDa, was produced at high purity, and exhibited excellent behavior. Importantly, YopM$^{\Delta N \Delta C}$
269 retained binding to recombinant hPYD as demonstrated by SEC co-elution (Fig. S7). Interestingly, co-
270 elution with hPYD did not significantly alter the SEC retention volume of the complex compared to
271 that of YopM$^{\Delta N \Delta C}$ on its own. In consideration of the aforementioned structural data, we hypothesized
272 that hPYD could 'tuck' into the concave surface of YopM$^{\Delta N \Delta C}$ without drastically increasing the
273 hydrodynamic radius of the nascent complex (Fig. S7A, C). Having verified the integrity of the binding
274 interaction, recombinant hPYD was then mixed with YopM$^{\Delta N \Delta C}$ in a 4:1 molar ratio for use in
275 crystallization trials, which led to a condition that produced suitable crystals (Fig. S6B).
276
277 In total, X-ray diffraction data were obtained from crystals produced using both strategies and the
278 resulting complexes were found to crystallize in different space groups: YopM$^{PestA}$ co-purified with
279 hPYD crystallized in space group *C* 2, and the YopM$^{\Delta N \Delta C}$-hPYD complex crystallized in space group
280 *P* $3_2$21 (Table 1). Although the former produced quality diffraction to 2.1 Å, it was apparent from the
281 electron density map that the C-terminal portion of YopM$^{PestA}$ beginning in the middle of LRR 9, as

well as the sixth α-helix of hPYD, were missing. Careful inspection of the crystal lattice led us to conclude that these missing regions could not be included without significant steric overlap with symmetry-related molecules. Based on these observations, we hypothesize that the fragments captured in this crystal were the result of an unanticipated limited proteolysis event, which is consistent with the difficulties in reproducing this crystal form. This complex is henceforth referred to as $YopM^{PestA}$*-hPYD*. In light of these observations, the co-crystal structure of $YopM^{\Delta N \Delta C}$-hPYD, which diffracted to 3.7 Å, was also refined and used to authenticate the limited proteolysis structure, which possessed the resolution necessary to confidently model the side-chain interactions at the binding interface.

With the exception of the truncations described above, the quaternary structures of both complexes are highly similar. The complex forms in a 1:1 stoichiometry with hPYD* nestled into the concave surface of $YopM^{PestA}$* (Fig 3A) and is consistent with the SEC co-elution profiles. Overall, the two $YopM^{PestA}$*-hPYD* molecules in the asymmetric unit are similar to each other ($C_\alpha$ RMSD = 0.6 Å), but hPYD α2, which lies near the binding interface, was observed in slightly different positions (Fig. S8A). This difference could be attributed to lattice packing, and alignment to the $YopM^{\Delta N \Delta C}$-hPYD complex identified "Molecule 1" as being most similar (compare Fig. S8B, $C_\alpha$ RMSD = 0.5 Å to Fig. S8C, $C_\alpha$ RMSD = 0.8 Å). Therefore, we conclude that the purported proteolytic truncation bears no influence on complex formation, and the biologically relevant interface is best interpreted from $YopM^{PestA}$*-hPYD* "Molecule 1," which was used for subsequent analyses as detailed below.

The co-crystallized complex reveals an extensive region of van der Waals contact, distributed across $YopM^{PestA}$* LRRs 1-9, the interacting residues of hPYD* are localized to α-helices 2-4, with α3 serving as a focal point (Fig. 3A). Detailed analysis of the contact surfaces suggests that electrostatic attraction is a driving feature of the $YopM^{PestA}$*-hPYD* interaction. The inner, concave surface of $YopM^{PestA}$* carries a uniform, negative charge (Fig. 3B). In contrast, the electrostatic surface potential of hPYD* is marked by both positive and negative patches. Notably, an equatorial and continuous band of positive charge is found on hPYD* that interfaces with the negatively charged, concave surface of $YopM^{PestA}$* (Fig. 3C). Although the interface is . In agreement with a binding interface that favors electrostatic complementarity, several extensive hydrogen-bond networks and salt bridges are observed (Fig. S10).

316 **Identification of YopM Residues Required for PYD Binding and Inhibition of the Human Pyrin**
317 **Inflammasome**
318
319 To identify residues on YopM$^{PestA}$ that are critical for hPYD binding, positions predicted by the
320 complex structure to be important for interaction were subjected to alanine substitution in groups of 3,
321 and the resulting variants were named Ala1-3 (Fig. S9A). The variants were tested for hPYD binding
322 by the BACTH assay, which indicated that Ala2 had significantly diminished binding whereas Ala1
323 and Ala3 retained binding to PYD at WT levels (Fig. S2B, Fig. S9B, Fig. 4A). Of the positions targeted
324 in Ala2, D159 and D161 are in LRR 5, while F177 is in LRR 6 (Fig. S9C). An analysis of the contact
325 frequency between YopM$^{PestA}$* and hPYD* for each interfacial residue is summarized in Fig. S10.
326 Although each YopM$^{PestA}$ Ala variant contains residues that make substantial contact with hPYD(Fig.
327 S10A), YopM$^{PestA}$* D159 and D161 also form a dense electrostatic network with hPYD* $\alpha$3 that
328 involves multiple hydrogen-bonds, two salt bridges, and coordination of a structural water (Figs. 3D,
329 3E, and S10B). The interactions made by YopM$^{PestA}$* F177 are entirely different, with the aromatic
330 side chain becoming shielded from bulk solvent by packing against hPYD* $\alpha$3 during binding (Fig.
331 3F). We purified the Ala2 variant of YopM$^{\Delta N\Delta C}$ (YopM$^{\Delta N\Delta C}$Ala2) from *E. coli* at similar yields as
332 YopM$^{\Delta N\Delta C}$. Analysis by SEC showed YopM$^{\Delta N\Delta C}$ Ala2 to be stable and eluted similarly to YopM$^{\Delta N\Delta C}$
333 (Fig. S11A,B vs Fig. S7A,B). When incubated at an equimolar ratio with purified hPYD and run on
334 SEC, YopM$^{\Delta N\Delta C}$Ala2 did not co-elute with hPYD as expected (Fig. S11C, D).
335
336 We also tested the impact of the Ala2 D159, D161 and F177 substitutions in the 15-LRR YopM$^{KIM}$
337 isoform. The sequence alignment of YopM$^{KIM}$ and YopM$^{PestA}$ shown in Fig. S12 indicates all three
338 positions are conserved. The Ala2 variant of YopM$^{KIM}$ displayed abolished binding to the hPYD in
339 BACTH (Fig. 4B, Fig. S2C).
340
341 We next expressed WT or Ala2 variants of YopM$^{KIM}$ and YopM$^{PestA}$ in *Yersinia* for functional studies. A
342 mutant *Y. pseudotuberculosis* strain (*yopJ*$^{C172A}$Δ*yopM*) was complemented with plasmids producing
343 the different YopM proteins under control of native promoters. The resulting strains were tested by
344 Yop secretion assay, which confirmed that the YopM Ala2 variants were released by the T3SS at
345 similar levels to WT, indicating that the amino-acid substitutions did not interfere with protein folding
346 or stability (Fig. S13A lanes 2-6). THP-1 human monocyte cells were infected with the *Y.*
347 *pseudotuberculosis* strains and we analyzed YopM translocation into the cells by immunoblotting, and
348 confirmed that the amino-acid substitutions did not impact injection by the T3SS (Fig. S13B lanes 1-
349 6). Pyrin inflammasome activation was measured in THP-1 cells infected with the *Y.*
350 *pseudotuberculosis* strains using immunoblotting and ELISA. We monitored the phosphorylation level

351 of pyrin at S242 by immunoblotting and found that the WT YopM proteins maintained total pyrin and
352 S242 phosphorylation, whereas in THP-1 cells infected with *Y. pseudotuberculosis* strains producing
353 the Ala2 variants there was reduced total pyrin and pyrin S242 phosphorylation levels (Fig. 4C lanes
354 1-6). As compared to the WT, both $YopM^{KIM}$ Ala2 and $YopM^{PestA}$ Ala2 were deficient for pyrin
355 inflammasome inhibition as measured by release of IL-1β from the THP-1 cells (Fig. 4D). Results of
356 colony-forming unit (CFU) assays performed on bacteria before and after infection indicated that the
357 THP-1 cells were not bactericidal (Fig.S14).
358
359 We then tested the contribution of individual codon changes in $YopM^{PestA}$ Ala2 on pyrin inflammasome
360 inhibition. We generated *Y. pseudotuberculosis yopJ*$^{C172A}$Δ*yopM* strains producing $YopM^{PestA}$ variants
361 containing alanine substitutions of each of the three residues individually (D159A, D161A or F177A)
362 in Ala2. The strains were tested for $YopM^{PestA}$ secretion as above, and normal levels were confirmed
363 (Fig. S13A lanes 7-9 vs lane 5). In the THP-1 infection assay the $YopM^{PestA}$ variants with single codon
364 changes were translocated at WT levels (Fig. S13B, lanes 7-9 vs lane 5). Mutation of D159 had the
365 strongest impact on the pyrin inhibiting activity of $YopM^{PestA}$, as pyrin dephosphorylation and IL-1β
366 release in THP-1 cells infected with this variant was similar to Ala2 or the empty vector control (Fig.
367 4C lane 7 and D). The D161 variant had an intermediate phenotype while mutation of F177 did not
368 have a major impact on $YopM^{PestA}$ pyrin inhibiting activity (Fig. 4C lanes 8,9 and D). These data
369 indicate that D159 is essential and D161 is important for $YopM^{PestA}$ to inhibit the human pyrin
370 inflammasome.
371
372
373 **Ala2 variants of $YopM^{KIM}$ and $YopM^{PestA}$ Inhibit the Mouse Pyrin Inflammasome**
374
375 Results of BACTH and GST pull down assays suggested that $YopM^{PestA}$ and $YopM^{KIM}$ bind with lower
376 affinity to mPYD than hPYD (Fig. 1B, Fig. S3). Based on this result, we hypothesized that binding to
377 mPYD is not required for YopM to target and inhibit mouse pyrin. Therefore, we tested whether YopM
378 Ala2 variants inhibit the pyrin inflammasome during *Y. pseudotuberculosis* infection of murine bone
379 marrow derived macrophages (BMDMs). $YopM^{KIM}$ and $YopM^{PestA}$ Ala2 variants were translocated into
380 infected BMDMs at WT levels (Fig. S13C). $YopM^{KIM}$ and $YopM^{PestA}$ Ala2 variants had only a subtle
381 defect in inhibiting IL-1β release from infected BMDMs, a phenotype that was not statistically
382 significant when compared to WT controls (Fig. S15). Figs. S10C and 10D show that in hPYD, R39,
383 R42 and S43 contribute to most of the interactions with $YopM^{PestA}$. The alignment of hPYD with
384 mPYD reveals that while R42 is conserved, position R39 is K39 (conservative change) and S43 is
385 G43 (non-conservative change) in mPYD (Fig. S16A). These and other differences in the binding

interface residues between hPYD and mPYD (Fig. S16A, B) are likely responsible for the weak interaction of the latter with YopM.

## Discussion

Here, we aimed to investigate the molecular mechanism of the YopM-pyrin interaction. Previous work showed that *Y. pestis* YopM binds human pyrin on the N-terminus that includes both the PYD and linker region (39). We found that *Y. pestis* YopM specifically binds the hPYD, and that the previously identified interaction with part of the linker (39) may have been affected by non-specific binding to GST. *Y. pestis* YopM binding to the hPYD was demonstrated *in vitro* using BACTH, GST pulldowns, and purified proteins. We also determined two co-crystal structures of $YopM^{PestA}$ bound to hPYD and identified residues on both proteins which participate in binding. We show that *Y. pestis* YopM variants which lose binding to hPYD *in vitro* can no longer inhibit the pyrin inflammasome in human monocytes infected with *Yersinia*. Taken together, these data suggest a model in which *Y. pestis* YopM hijacks host kinases RSK and PRK, binds to the hPYD as a targeting site and promotes pyrin inactivation by phosphorylation of the linker (Fig. S1C).

The $YopM^{PestA}$*-hPYD* complex is an additional notable structure of a virulence factor targeting a member of the death domain fold (DDF) family of proteins (50). Enteropathogenic *Escherichia coli* encodes T3SS effector NleB, which attaches N-acetylglucosamine to the death domain of FADD or TRADD, preventing interaction with death receptors and assembly of death receptor complexes (50).

The DDF family is comprised of four sub-groups; death domain (DD), death effector domain (DED), caspase activation and recruitment domain (CARD) and pyrin domain (PYD) (51). Members of this family play roles in cytosolic innate immune and cell death pathways (51). All DDF proteins participate in homotypic protein-protein interactions resulting in the assembly of higher-order oligomers (51). DDF proteins have a conserved Greek key motif comprising of six $\alpha$-helices with variations in the helices defining the sub-families (51). PYDs stand out in this superfamily because they have the shortest helix 3, which is also preceded by a long unstructured α2-α3 loop (52, 53). Helix 3 and the unstructured α2-α3 loop have been hypothesized to play a role in protein-protein interactions of PYDs (52, 53). Intriguingly, R42 located in α3 is predicted to be a key residue involved in YopM binding, alongside R39, which is located on the α2-α3 loop. R42 was proposed to act as a conformational switch due to the unstructured nature of α-3 and the proximal α2-α3 loop (52).

The complex structure presented here reveals a strong charge complementarity between $YopM^{PestA}$* and hPYD*. This is not surprising, given that the concave surface of $YopM^{PestA}$*is negatively charged

421 (Fig. 3B) and the hPYD* has both positively and negatively charged surfaces. Three negatively
422 charged residues on YopM$^{PestA*}$ (D159, D161 and D203) were predicted from the complex to
423 contribute to hPYD* binding. YopM$^{PestA*}$ D159 and D161 are located in LRR 5 while D203 is in LRR 7.
424 Substitution of YopM$^{PestA*}$ D159 had a strong negative impact on hPYD binding and this could be
425 because it forms hydrogen bonds with R42 and S43 and is also facilitating hydrogen bonds with one
426 of the structural waters observed at the YopM$^{PestA*}$-hPYD* interface (Fig 3D). Surprisingly, YopM$^{PestA*}$
427 D161 makes extensive interactions with hPYD*, forming two salt bridges with hPYD* R39 and R42
428 (Fig 3E), yet the impact of its mutation was intermediate. This might be because the same hPYD
429 residues make more interactions with other YopM residues, hence only dampening rather than
430 abolishing the interface. Substitution of YopM F177 had minimal impact on the inhibitory activity of
431 YopM and is unsurprising given the interaction is restricted to more superficial van der Waals
432 contacts with hPYD (Fig 3F). Three residues on YopM$^{PestA*}$ (N120, Y135 and N140) are also
433 predicted to contribute extensive van der Waals interactions and hydrogen bonds yet simultaneously
434 mutating them (Ala1) had no impact on hPYD binding in BACTH. These results could indicate that the
435 overall impact of losing these interactions in the Ala1 variant is minimal, and that YopM relies more on
436 the centrally located acidic residues targeted in Ala2.
437 Our results indicate that most of the concave surface of the YopM LRR domain is sterically occluded
438 when bound to hPYD. YopM LRRs 6-15 have been implicated in binding to PRK (40). If PRK also
439 binds to the concave surface of the YopM LRR domain, binding to the PRK kinase domain and hPYD
440 would be mutually exclusive. As shown in Fig. S1C, PRK may need to be released to allow YopM to
441 target the hPYD and use hijacked RSK to phosphorylate the human pyrin linker. Additional studies
442 are needed to understand if binding of PRK and hPYD to YopM are mutually exclusive.
443 PYDs are known to interact through electrostatic interactions (53, 54). Critical to assembly of the pyrin
444 inflammasome is an interaction between the pyrin and ASC PYDs (53) which then allows a
445 recruitment of pro-caspase-1 (55). The two PYDs interact using complementary positive and
446 negatively charged sites (53). Additionally, because these PYDs have multiple charged surfaces, they
447 can simultaneously self-associate and participate in inter-molecular interactions, leading to the
448 assembly of a multi-protein complex (53). Vajjhala et al. identified 3 and 2 binding sites on pyrin and
449 ASC PYDs, respectively (53). R42 of pyrin PYD and R41 of ASC PYD, which are in α3, and in site #2
450 for each protein, were identified to be important for binding to each other (53). The finding that YopM
451 specifically binds to the positively charged patch of hPYD containing R42 and representing site #2 is
452 intriguing, given that it overlaps with an ASC binding site and the B-box binding site (53). This might
453 indicate that YopM evolved to target a specific binding region on hPYD essential for its function.

454 Additionally, YopM may have to compete with ASC and the B-box to bind hPYD. Future studies that
455 define hPYD interactions with the B-box, ASC and YopM will be informative in testing this hypothesis.
456

457 Naturally occurring codon changes R39G or R42W in hPYD have been implicated in causing Familial
458 Mediterranean fever (FMF), although neither mutation has been validated to be disease causing (56).
459 FMF is an autoinflammatory disease resulting from gain of function mutations in the pyrin gene *MEFV*
460 (25). People with FMF experience recurring episodes of fever with inflammation of serosal membranes
461 in the abdomen, lungs and heart (25). Most pathogenic FMF codon changes are located on the C-
462 terminal B30.2 domain (25, 56). Results of population genetic analysis are consistent with the
463 hypothesis that historic plague epidemics in the Mediterranean selected for FMF gain of function codon
464 changes in the B30.2 domain (39). The impact of the R42W substitution on hPYD structure and function
465 has been studied, and it was found to increase the stability of the short helix 3 (53). While
466 counterintuitive, this increased structural stability might be deleterious to the function of hPYD, due to
467 the importance of flexibility in this region. The R42W substitution appeared to cause a greater reduction
468 in binding of hPYD to the B-box as compared to ASC (53). The R42W substitution may reduce negative
469 regulation by the B-box (31) which in turn could increase activation of pyrin (53). It is possible that the
470 R42W substitution also reduces YopM binding to hPYD, which would limit pyrin inactivation during
471 *Yersinia* infection. Additional experiments are needed to understand how the R42W and R39G
472 substitutions in hPYD impact YopM and B-box binding, pyrin activation and *Yersinia* pathogenesis.
473

474 The finding that *Y. pestis* YopM does not strongly bind to mPYD could mean that this domain has
475 evolved reduced affinity for recognition. This is possible, given that rodents have likely been hosts for
476 *Y. pestis* longer than humans. Human and mouse PYDs have a sequence identity of 76% and amino
477 acid differences between the two could indicate sites of positive selection on mPYD. hPYD R39, R42
478 and S43 have the most interactions with YopM and two of these sites have conservative (R39 to K39)
479 or non-conservative (S43 to G43) changes in mPYD. These substitutions could be sufficient to disrupt
480 YopM binding. The R47M change in mPYD could also interfere with the band of positively charged
481 surface residues seen in hPYD. Given that there are only three positively charged residues in the
482 YopM binding region (R39, R42 and R47), the loss of one of them might have a disproportionate
483 impact especially because the PYD is small. Additionally, because the three substituted residues are
484 located on $\alpha$3, they might be causing structural changes that decrease recognition by YopM. These
485 three residues might be the hotspots of mPYD evolution, but a more detailed analysis of positive
486 selection in mouse pyrin would be informative in testing this hypothesis. There is evidence that a
487 small number of residue substitutions can have a significant impact on the interactions of host-

488 pathogen proteins (57). These residues function as hotspots in the host-pathogen arms race (57). It is
489 therefore plausible that a change in three residues in mPYD would significantly diminish binding with
490 YopM.
491
492 Despite the loss of stand-alone mPYD binding, we found that *Y. pestis* YopM Ala2 variants retain the
493 ability to inhibit the pyrin inflammasome in infected mouse macrophages. These results suggest that
494 YopM targets and inhibits murine pyrin independent of the PYD. PRK was shown to be important for
495 YopM to inhibit the pyrin inflammasome in mouse macrophages infected with *Y. pseudotuberculosis*
496 (15). PRK uses its kinase domain to target and phosphorylate pyrin (33, 39). One possibility is that
497 YopM uses hijacked PRK to target and phosphorylate murine pyrin (Fig. S1C). Further studies that
498 focus on how YopM targets and inhibits mouse pyrin are needed to better understand differences in
499 this key mechanism of pathogenesis in murine vs human cells.
500
501 **ACKNOWLEDGMENTS AND FUNDING**
502
503 Supported by NIH grants R01-AI099222 (to JB), P20-GM113132 (bioMT cores; to DM), and T32-
504 AI007519 (training grant stipend to ARS).
505
506 This research used 17-ID-1 of the National Synchrotron Light Source II, a U.S. Department of Energy
507 (DOE) Office of Science User Facility operated for the DOE Office of Science by Brookhaven National
508 Laboratory under Contract No. DE-SC0012704. The Center for BioMolecular Structure (CBMS) is
509 primarily supported by the National Institutes of Health, National Institute of General Medical
510 Sciences (NIGMS) through a Center Core P30 Grant (P30GM133893), and by the DOE Office of
511 Biological and Environmental Research (KP1605010).
512
513 **MATERIALS AND METHODS**

514 **Protein expression vectors and bacterial host strains**

515 The vectors and bacterial host strains used are provided in Table 2. In brief, YopM$^{PestA}$ constructs were
516 cloned as N-terminal hexahistidine-GST (6xHisGST) fusions. In addition to the full-length coding
517 sequence (6xHisGST-YopM$^{PestA}$) that was cloned into a modified pGEX_KT vector, a truncated
518 construct lacking the disordered N- and C-terminal extensions (residues 34-344, YopM$^{\Delta N \Delta C}$) was cloned
519 into a pET28-derived expression vector. These extensions were excluded from the final construct to
520 mitigate potential interference during crystallization trials. The CDS of the human PYD (residues 1-90,
521 herein referred to as hPYD) was cloned as either an N-terminal hexahistidine fusion in a pDuet vector,
522 or as a C-terminal octahistidine fusion in a pET28a vector. All inserts were first PCR amplified then

523 inserted into their respective vectors by either restriction cloning using BamHI and EcoRI sites or using
524 the NEB Gibson Assembly kit according to the manufacturer's recommendations.

525 **Bacterial Two Hybrid Assay**

526 PYDs and pyrin linker constructs were expressed from pUT18 with C-terminal fusions of T18 and
527 YopM isoforms and variants were expressed from pKT25 with N-terminal fusions to T25. The assay
528 was performed as previously described (58, 59). Briefly, electrocompetent BTH101 *E. coli* cells were
529 co-transformed with each vector or empty vector controls and recovered in 250ul SOC media at 37°C.
530 Cells were plated on an Ampicillin (Amp) or Carbencillin(Carb) + Kanamycin(Kan) plate for 2 days at
531 30°C and resulting colonies streaked onto Amp/Carb + Kan + isopropyl β-D-1-thiogalactopyranoside
532 (IPTG) plates with and without X-Gal. After 1 day at 30°C the cells on plates without X-Gal were
533 scraped off and resuspended in Phosphate Buffered Saline (PBS; 140 mM NaCl, 2.68 mM KCl, 8.1
534 mM $Na_2HPO_4$, 1.47 mM $KH_2PO_4$) and normalized to $0.D_{600}$ ~ 0.5. The cells were then incubated at
535 30°C for 5 min for lysis with 25 µl of 0.1% SDS, 50 µl chloroform in Z buffer (60 mM $Na_2HPO_4$, 40
536 mM $NaH_2PO_4$,10 mM KCl, 1 mM $MgSO_4$) with 50 mM β-mercaptoethanol (β-ME). 200 µl of 4 mg/mL
537 ONPG in Z buffer was added to the cells and the reaction performed for 5 minutes at 30°C. A 500 µl
538 solution of 1M sodium bicarbonate was added to stop the reaction and the absorbance was
539 measured at 420 and 550 nm. The β-galactosidase activity was then calculated using the following
540 formula as described by Miller:

541 Miller Units $=1000*[(OD_{420} – 1.75*OD_{550})/ (\text{time in minutes}*OD_{600}*\text{volume of scraped cultures})]$

542 **GST Pulldown Assay**

543 GST-YopM and His-tagged murine or human PYDs were co-expressed in *E. coli* BL21 cells. The
544 bacterial lysates were prepared with BugBuster Protein Extraction Reagent (Millipore) in PBS and
545 supplemented with lysonase (Millipore) and Roche complete mini protease inhibitor. Lysates were
546 then incubated with GST resin (GST.Bind, Millipore) overnight. The resin was then washed and
547 proteins eluted using 1X sample buffer and analyzed on SDS-PAGE gels followed by blue staining or
548 α-His immunoblotting. Immunoblotting procedures are described below.

549 **Protein Expression and Purification**

550 All recombinant proteins used in this manuscript were expressed in BL21(DE3) cells. Proteins were
551 either co-expressed and co-purified for crystallization of the the $YopM^{PestA}$-hPYD* structure or
552 individually prepared for the $YopM^{\Delta N \Delta C}$-hPYD complex. In all preparations, cells were grown in Terrific
553 Broth (TB) at 37°C for 2-3 hours until an $O.D._{600}$ of ~ 1 was achieved. Cells were induced with 0.1 mM

554 IPTG and protein expression was allowed to proceed at 18°C for 16-18 h. For YopM, induced cells
555 were allowed to express protein at 37°C for 4 h. Cells were harvested by centrifugation at 4,200 x *g* at
556 4°C for 15 min. Cells were resuspended in lysis buffer (150 mM NaCl, 1 mM Tris(2-
557 carboxyethyl)phosphine hydrochloride (TCEP), and 20 mM Tris, pH 7.4) supplemented with Roche
558 complete mini EDTA (ethylenediaminetetraacetic acid) protease inhibitor and Lysonase Bioprocessing
559 Reagent from Millipore Sigma and lysed using an LM10 microfluidizer. The insoluble fraction was
560 separated by centrifugation using a Ti 45 Rotor in a Beckman Ultima L-70 ultracentrifuge at 40,000
561 rpm for 1 h at 4°C. For both the $YopM^{PestA}$ only construct and $YopM^{PestA}$ co-expressed with hPYD,
562 recombinant protein was captured on GST resin and eluted by on-column proteolysis using the
563 Tobacco Etch Virus (TEV) protease in buffer composed of 150 mM NaCl, 1 mM TCEP, and 20 mM
564 Tris, pH 7.4. For YopM co-purified with hPYD, the hexahistidine tag on hPYD was cleaved using the
565 HRV-3C protease during dialysis against buffer containing 150 mM NaCl, 1 mM TCEP, and 20 mM
566 Tris, pH 7.4; cleavage and dialysis were allowed to proceed overnight at 4°C. In both cases,
567 recombinant protein was further purified by size exclusion chromatography (SEC) using a HiLoad
568 Superdex 200 26/600 PG column and fractions containing purified protein, as assessed by reducing
569 SDS-PAGE, were pooled and concentrated.

570 For the $YopM^{\Delta N \Delta C}$ -hPYD complex structure, proteins were individually expressed and purified. The
571 bacterial pellets were expressed, lysed, and clarified as described above except using 20 mM 4-(2-
572 hydroxyethyl)-1-piperazineethanesulfonic acid (HEPES), pH 7.4 buffer system in place of Tris.
573 Clarified lysates were applied to a 5 mL His-TRAP column then washed with buffer composed of
574 500mM NaCl and 20 mM Tris, pH 8.0 supplemented with imidazole concentrations ranging from 10 –
575 50 mM. Proteins were eluted by gradient elution ranging from 10-250 mM imidazole. For the hPYD
576 preparation, fractions containing protein were pooled, concentrated and run on a HiLoad Superdex
577 200 26/600 PG column in buffer composed of 150 mM NaCl, 1mM TCEP, and 20 mM HEPES, pH
578 7.4. For $YopM^{\Delta N \Delta C}$, fractions containing recombinant protein were pooled and TEV cleavage reactions
579 were set up during simultaneous dialysis against buffer composed of 150 mM NaCl, 1 mM TCEP, and
580 20 mM HEPES, pH 7.4 at 4°C, for 16 – 18 h. Cleaved protein was further purified by cation exchange
581 using SP Sepharose and IMAC using Ni-NTA resin. Finally, samples were purified by SEC using a
582 HiLoad Superdex 200 26/600 PG column.

583 **Analytical SEC and SEC-MALS**

584 Analytical SECwas performed on a Superdex 200 10/300 column attached to an AKTA pure protein
585 purification system (GE healthcare). Samples were analyzed in 150 mM NaCl, 1 mM TCEP, and 20

586 mM Tris, pH 7.4for GST resin purified YopM$^{PestA}$ and YopM$^{PestA}$-hPYD. YopM$^{\Delta N \Delta C}$ and YopM$^{\Delta N \Delta C}$ hPYD
587 complex were analyzed in 150 mM NaCl, 1 mM TCEP, and 20 mM HEPES, pH 7.4. Analytical SEC
588 was performed at 0.75 mL/min. The column was calibrated using the 29,000-700,000 Da gel filtration
589 markers kit from Millipore Sigma (MWG1000F) containing the following molecular mass standards:
590 Blue Dextran (2,000 kDa), Apoferritin (440 kDa), β-Amylase (200 kDa), Alcohol Dehydrogenase (150
591 kDa), Albumin (66 kDa), Carbonic Anhydrase (29 kDa).

592 For SEC-MALS, an AKTAPure instrument (Cytiva) coupled to an Optilab refractive index detector
593 (Wyatt) and light-scattering detector (Wyatt MiniDawn Tristar) were used. SEC was performed using a
594 Superose 10/300 Column at 0.5 mL/min and the laser wavelength was set to 690 nm. The molar
595 mass was determined using the ASTRA software package (Wyatt).

596 **Velocity Ultracentrifugation**

597 Analytical ultracentrifugation was conducted using a Beckman Proteomelab XL-A and an AN-60 rotor.
598 For sedimentation velocity analytical ultracentrifugation, YopM$^{PestA}$ in 150 mM NaCl, 1 mM TCEP, with
599 either 20 mM Tris, pH 7.4 or 20 mM MES pH 5.0 was centrifuged at 35,000 rpm with monitoring at
600 280 nm. Data were analyzed using Sedfit (60) to determine sedimentation coefficient, frictional ratio,
601 and apparent mass, as described elsewhere (61). The sedimentation coefficient reported is that of the
602 major peak (at least 80% of the total analyzed mass) at $OD_{280}$ for each sample.

603 **Crystallization**

604 The YopM$^{PestA}$*-hPYD* complex was crystallized using the co-purified YopM-hPYD. The complex was
605 crystallized by vapor diffusion in 4 µL sitting drops composed of well solution (12% [*w/v*] PEG 4K, 40
606 mM MES, pH 5.0) and co-purified YopM$^{PestA}$-hPYD at a concentration of 6.5 mg/mL as determined by
607 the Bradford assay; drops were set at a 1:1 ratio. Prior to harvesting, crystals were cryoprotected in
608 well solution supplemented with 20% (*v/v*) glycerol then flash cooled in liquid nitrogen.

609 For co-crystallization of the YopM$^{\Delta N \Delta C}$-hPYD complex, the purified YopM$^{\Delta N \Delta C}$ was first combined with
610 purified hPYD in a 1:4 molar ratio at a final total protein concentration of 1.2 mg/mL. Suitable crystals
611 were obtained by vapor diffusion in 4 µL hanging drops composed of well solution (19% [*w/v*] PEG
612 3350, 300 mM NaSCN, and 100 mM Bis-Tris Propane, pH 6.5) and protein set at a 1:1 drop ratio.
613 Crystals were harvested and flash cooled as described above.

614 **Structure Determination and Refinement**

615 For both co-crystal structures, data were collected at the National Synchrotron Light Source II on the
616 AMX beamlines (17-ID-1) using a Dectris 9M pixel detector. For the full-length co-purified YopM$^{PestA*}$-

617 hPYD* complex, 180° of rotation X-ray diffraction data were collected using 0.1° per frame. For the
618 YopM$^{\Delta N \Delta C}$-hPYD complex, 120° of rotation X-ray diffraction data were collected using 0.2° per frame.
619 The diffraction images were reduced using XDS and scaled using XSCALE (62). The $R_{free}$ set was
620 generated from 5% of reflections in the thin resolution shells using Phenix reflection file editor. The
621 Matthews coefficient was determined using the CCP4 supported program MATTHEWS_COEF (65).
622 In both cases, structures were solved by molecular replacement using PHASER-MR and
623 iterative automated and manual refinements were carried out using phenix.refine and Coot,
624 respectively. Specific details pertaining to the phasing and refinement of each structure follows.
625
626 For the YopM-hPYD*, initial phase estimates were obtained using the crystal structure of NLRP9 PYD
627 (pdb_00006z2g) as a search model. For the 13-LRR YopM$^{PestA}$ isoform used in these studies, a
628 composite model was initially created using the crystal structure of a related 15-LRR *Y. pestis* YopM
629 isoform (pdb_00001g9u) in PyMol to omit additional leucine rich repeats in the central LRR domain.
630 Following molecular replacement, negative density peaks were observed in the m*Fo* – d*Fc* map along
631 the entirety of the C-terminal portion of YopM. After omission of the region spanning residues 248-344
632 followed by iterative automated and manual refinements using PHENIX.REFINE. and Coot,
633 respectively, it was determined that a YopM truncation was captured in the crystal lattice. We posit a
634 limited proteolysis event occurred in the mother liquor preceding nucleation that resulted in a shortened
635 YopM in the co-purified YopM-hPYD construct represented in the deposited coordinates. This
636 conclusion is supported by the inability of the missing YopM sequence to be included in either molecule
637 of the asymmetric unit without incurring severe steric overlap with molecules related by both
638 crystallographic and non-crystallographic symmetry. A region spanning residues 79-90 and
639 encompassing the last $\alpha$-helix of hPYD is also absent in this crystal structure and is presumed to be
640 another target of errant proteolytic activity. Additionally, a > 4 sigma positive density peak adjacent to
641 the sulfhydryl group of Cys100 of Chain B was observed that exhibited good fitment to a carboxymethyl
642 cysteine. However, LC-MS/MS analysis of crystals rehydrated from neighboring drops with similar well-
643 solution compositions failed to corroborate the observations in the crystallographic data despite
644 evidence for low-abundance carboxymethylation at other cysteines. The positive density peak was
645 therefore left unmodeled. Anisotropic refinement of protein atoms was carried out using one TLS group
646 per chain; subsequent refinements transpired without incident.
647
648 For the co-crystal structure of the YopM$^{PestA*}$-hPYD* complex, initial phase estimates were obtained
649 using a model composed of the refined YopM-hPYD structure described above with a graft of the C-
650 terminal portion of the aforementioned *Y. pestis* YopM isoform (pdb_00001g9u, residues 286-396). The

651 graft was created by least-squares superposition of the preceding two LRRs with the corresponding
652 region of the solved YopM-hPYD complex. Due to the low resolution and map quality, automated
653 refinements were performed using secondary structure restraints. The refined coordinates of the YopM-
654 hPYD complex were also used to impose reference model restraints during automated refinement but
655 were lifted for the final stages.

656 **Accession Numbers**

657 The coordinate files and structure factor files for both co-crystal structures solved herein are available
658 at the Protein Data Bank (66) using the following codes: pdb_00009oyu (YopM-hPYD) and
659 pdb_000010dr (YopM$^{\Delta N \Delta C}$-hPYD). Rotation X-ray diffraction image files were uploaded to the SBGrid
660 Data Bank and are searchable by PDB codes.

661 **Structural Analyses and Visualization**

662 Structural analyses were performed using PyMol (67) and the CCP4 Suite (68) as part of the SBGrid
663 software environment (69). Structural alignments were performed in PyMol using all $C_\alpha$ of the YopM
664 chains for each complex. The Adaptive Poisson-Boltzmann Solver (70) (APBS) plugin was used to
665 calculate electrostatic surface potentials for YopM and hPYD in PyMol. All structural figures were
666 rendered using PyMol. Residues at the binding interface were identified using the CCP4 supported
667 program CONTACTS (68) with a 5 Å cutoff, and histograms displaying per-residue contacts were
668 created using R (71) with the following packages: tidyverse (72), ggprsim (73), and ggplot2 (74).

669 **Construction of *Y. pseudotuberculosis* strains**

670 *Y. pseudotuberculosis* strains expressing different YopM isoforms and variants (see Table 2) were
671 generated by conjugating donor *E. coli* S17 lambda-pir containing the pMMB67EH plasmid plus YopM
672 isoforms/variants with a *Y. pseudotuberculosis* strain lacking the *yopM* gene and harboring the catalytic
673 mutation in YopJ (mJ*ΔyopM*).

674 **Yop Secretion Assay**

675 *Y. pseudotuberculosis yopJ$^{C172A}$ΔyopM* strains were inoculated into LB Amp and grown with shaking
676 at 28°C. Overnight cultures of *Yersinia* were diluted 1:40 in LB media containing 20 mM sodium
677 oxalate and 20 mM $MgCl_2$ and grown for 2 h at 28°C then shifted to 37°C for 4 h. Supernatants were
678 precipitated using trichloroacetic acid (TCA) overnight. Precipitated proteins were centrifuged at
679 14,000 rpm for 30 min, and the resulting pellet washed with acetone. The protein pellets were
680 resuspended in 100 µl 1X sample buffer and 10 µl of the samples were run on 4–12% NuPAGE Bis-

681 Tris SDS-PAGE gels (Invitrogen by ThermoFisher Scientific). The gels were stained using One-Step
682 Blue Protein Gel Stain (Biotium) and imaged on an iBright FL1500 imager (ThermoFisher Scientific).

683 **THP-1 Cells Tissue Culture and Infections**

684 THP-1 human monocyte cells (ATCC TIB-202) were grown in filter-sterilized RPMI-1640 media with
685 10% heat-inactivated fetal bovine serum (FBS), 0.05 mM β-MEand 1% pen-strep (10,000 U/mL
686 Penicillin + 10,000 µg/mL streptomycin, Gibco) in 25 $cm^2$ flasks. Once the cells reached confluency,
687 they were split into 75 $cm^2$ flasks. For infections, $0.8x10^6$ total cells per well were seeded in 1.5 mL
688 serum-free media in 6-well plates. Overnight cultures of *Yersinia* were diluted 1:40 in LB media
689 containing 20 mM sodium oxalate and 20 mM $MgCl_2$ and grown for 1 h at 28°C, then shifted to 37°C
690 for 2 h. Cultures were centrifuged and the bacterial pellets washed in 1X PBS. Resuspended bacteria
691 were then mixed with cells at a multiplicity of infection (MOI) of 30 in serum-free media then plated on
692 6-well plates. After infection for 4 h at 37°C in 5% $CO_2$, the cell contents were collected and
693 centrifuged for 15 min at 14,000 rpm. The supernatants were collected for IL-1β analysis by ELISA
694 (see below). The cell pellet was then washed with 1X Hanks balanced salt solution (HBSS) and lysed
695 for immunoblot analysis as described below. Samples of bacteria inoculated into each well at t=0 h
696 were serially diluted and plated for CFU quantification. Total bacterial-monocyte co-cultures were
697 solubilized in 0.1% NP-40 detergent (t=4 h) followed by serial dilutions and plating to determine CFU
698 recovery post-infection.

699 **BMDM Cells Tissue Culture and Infections**

700 BMDMs were obtained from femurs and tibia of 8-week-old WT C57BL/6 mice (Jackson Laboratories)
701 and cultured as previously described (75). After differentiation for 7 days, the BMDMs were seeded in
702 3 mL MGM 10/10 containing Dulbecco's modified Eagle Medium (DMEM) plus GlutaMAX (Gibco),
703 10% (*v/v*) heat-inactivated FBS (GE HealthCare), 10% (*v/v*)L929 cell-conditioned medium, 1 mM
704 sodium pyruvate (Gibco), and 10 mM HEPES (Gibco) at a density of $0.8x10^6$ cells/well. The cells
705 were allowed to settle for at least 1 h then primed overnight by addition of 100 ng/mL O26:B6 *E. coli*
706 LPS (Sigma) in 1X PBS. *Yersinia* strains were grown as described above and added to serum-free
707 MGM 10/10. MGM 10/10 with or without bacteria at an MOI of 30 was added to the wells of primed
708 macrophages. Plates were centrifuged for 5 min at 112 X g to facilitate *Yersinia* contact with cells and
709 incubated for 90 min at 37°C in 5% $CO_2$. Following the infection, cell supernatants were collected for
710 IL-1β analysis by ELISA and cells lysed for immunoblot analysis (see below).

711 **THP-1 and BMDM Lysates and Immunoblotting**

712 THP-1 and BMDM cells were lysed in mammalian protein extraction reagent (MPER, Thermo
713 Scientific) supplemented with protease inhibitor cocktail and phosphatase inhibitor (Roche). The
714 lysates were spun down to separate out soluble from insoluble fractions. Protein concentration levels
715 were measured using the bicinchoninic acid assay (BCA, Thermo Fisher Scientific). 5-10 µg total
716 soluble protein lysate was run on 4–12% NuPAGE Bis-Tris SDS-PAGE gels (Invitrogen by
717 ThermoFisher Scientific) and transferred to polyvinylidene difluoride membranes (ThermoFisher
718 Scientific) using an iBlot 3 gel transfer device (Life Technologies). Membranes were blocked using 5
719 % (*w/v*) nonfat dairy milk (Lab Scientific bioKEMIX) for 1 h at room temperature before incubation with
720 primary antibody overnight. Primary antibodies used in this study include rabbit-anti-mouse phospho-
721 serine 241 monoclonal antibody (1:1,000 dilution, Ab201784; Abcam), rabbit anti-human pyrin
722 monoclonal ( 1:1,000, Cell Signaling #58525 and #40649), rabbit-anti-mouse/human polyclonal β-
723 actin (1:1,000 # 4967; Cell Signaling), rabbit anti-*Y. pestis* YopM polyclonal (1:10,000 dilution,
724 antibody provided by Susan Straley) and mouse anti-HIS tag monoclonal (1:5,000 dilution, # MMS-
725 156P BioLegend). Horseradish peroxidase-conjugated anti-rabbit or anti-mouse (Jackson Laboratory)
726 were used as secondary antibodies. Protein bands bound by antibodies were visualized using
727 chemiluminescent detection reagent (GE Healthcare) on an iBright FL1500 imager (ThermoFisher
728 Scientific). Band quantification was also performed on the iBright FL1500 imager.

729 **IL-1β Quantification**

730 Levels of IL-1β in THP-1 and BMDM supernatants were quantified using human (RandD Systems)
731 and mouse (MLB00C, RandD Systems) ELISA kits respectively, following the manufacturer's
732 instructions.

733 **Statistical Analysis**

734 GraphPad Prism was used to perform statistical analyses. Significance was determined by one-way
735 ANOVA and Tukey's *post hoc* tests performed for BACTH and ELISA experiments.

736

737

| **Table 1. Summary of data collection, reduction, and refinement statistics** | | |
|---|---|---|
| | YopM$^{PestA}$*-hPYD* | YopM$^{\Delta N \Delta C}$-hPYD |
| **Data Collection** | | |
| Beamline | NSLS-II 17-ID-1 | NSLS-II 17-ID-1 |
| Wavelength (Å) | 0.97933 | 0.920105 |
| Space Group | *C* 2 | *P* $3_2$21 |
| Unit cell parameters | | |
| *a, b, c* (Å) | 166.2, 41.6, 115.0 | 141.6, 141.6, 61.6 |
| $\alpha, \beta, \gamma$ (°) | 90, 132.7, 90 | 90, 90, 120 |
| Resolution[a] (Å) | 39.4 - 2.10 (2.18 - 2.10) | 30.7 - 3.70 (3.83 - 3.70) |
| $R_{meas}$[b] (%) | 5.3 (30.8) | 8.4 (83.9) |
| $R_{p.i.m.}$ (%) | 2.9 (18.0) | 4.6 (47.1) |
| $CC_{1/2}$[c] (%) | 99.9 (94.8) | 99.8 (43.4) |
| $I/\sigma_I$ | 14.0 (3.3) | 8.9 (1.4) |
| Completeness (%) | 98.9 (94.6) | 96.6 (98.7) |
| Redundancy | 3.3 (2.6) | 3.1 (2.9) |
| **Refinement** | | |
| #Total reflections | 33962 (3229) | 7525 (774) |
| Test-set reflections | 1664 (159) | 407 (43) |
| $R_{work}$[d]/$R_{free}$[e] (%) | 18.2/21.2 | 23.9/25.0 |
| Number of atoms: | | |
| Protein | 4601 | 3140 |
| Water | 240 | 0 |
| Ramachandran Plot[f] (%) | 95.5/4.5/0.0 | 94.8/5.2/0.0 |
| $B_{average}$ (Å$^2$) | 50.3 | 145.5 |
| Protein | 50.6 | 145.5 |
| Water | 44.4 | |
| Bond length RMSD (Å) | 0.007 | 0.003 |
| Bond angle RMSD (°) | 0.82 | 0.71 |
| **PDB ID** | pdb_00009oyu | pdb_000010dr |

738 [a] Values in parentheses correspond to the highest resolution shell.

739 [b] $R_{meas}$: the redundancy independent R-factor, described in reference (76).

740 [c] $CC_{½}$: the percentage of correlation between intensities from random half-datasets (77).

741 [d] $R_{work} = \Sigma_h |F_{obs}(h) - F_{calc}(h)|/\Sigma_h F_{obs}(h)$, $h \in$ [working set]

742 [e] $R_{free} = \Sigma_h |F_{obs}(h) - F_{calc}(h)|/\Sigma_h F_{obs}(h)$, $h \in$ [test set]

743 [f] Favored/allowed/outliers

744

745

| Table 2. Vectors Name | Bacterial host strain | Description or insert | Reference |
|---|---|---|---|
| pUT18 | BTH101 | pUT18 empty vector allowing fusion to the N-terminus of the cya T18 fragment | Euromedex |
| pKT25 | BTH101 | pKT25 empty vector allowing fusion to the C-terminus of the cya T25 fragment | Euromedex |
| pKT25_YopM$^{PestA}$ | BTH101 | Full-length YopM$^{PestA}$ CDS | This study |
| pKT25_YopM$^{PestA}$ Ala1 | BTH101 | YopM$^{PestA}$ Ala1 (N120A, Y135A, and N140A) | This study |
| pKT25_YopM$^{PestA}$ Ala2 | BTH101 | YopM$^{PestA}$ Ala2 (D159A, D161A, and F177A) | This study |
| pKT25_YopM$^{PestA}$ Ala3 | BTH101 | YopM$^{PestA}$ Ala3 (Y201A, N221A, and E279A) | This study |
| pKT25_YopM$^{KIM}$ | BTH101 | Full-length YopM$^{KIM}$ CDS | This study |
| pKT25_YopM$^{KIM}$ Ala2 | BTH101 | YopM$^{KIM}$ Ala2 (D159A, D161A, and F177A) | This study |
| pUT18_hPYD | BTH101 | Human pyrin aa 1-90 | This study |
| pUT18_mPYD | BTH101 | Mouse pyrin aa 1-90 | This study |
| pUT18_hPyrin186-326 | BTH101 | Human pyrin aa 186-326 | This study |
| pKT25_ZIP | BTH101 | Leucine zipper | Euromedex |
| pUT18C_ZIP | BTH101 | Leucine zipper | Euromedex |
| pGEX_2T | BL21 | pGEX_2T empty vector allowing fusion to the C-terminus of the GST tag | Chung et al 2016 |
| pGEX_2T_YopM$^{KIM}$ | BL21 | Full-length YopM$^{KIM}$ CDS | Chung et al 2016 |
| pACYCDuet_hPYD | BL21 | Human pyrin aa 1-90 | This study |
| pACYCDuet_mPYD | BL21 | Mouse pyrin aa 1-90 | This study |
| pGEX_KT_YopM$^{PestA}$ | BL21 | Full-length YopM$^{PestA}$ CDS in a modified pGEX_KT vector with a 6XHIS and TEV site downstream of the thrombin site | This study |
| pET_6XHIS_GST_TEV_M$^{\Delta N \Delta C}$ | BL21 | YopM$^{PestA}$ aa 34-344 | This study |

| | | | |
|---|---|---|---|
| pET28A_ hPYD _8xHIS | BL21 | Human pyrin aa 1-90 in a modified pET28A vector with an 8X HIS tag | This study |
| pMMB67EH_YopM$^{PestA}$ WT | *Y. pseudotuberculosis* mJΔyopM | Full-length YopM$^{PestA}$ CDS | This study |
| pMMB67EH_YopM$^{PestA}$ Ala1 | *Y. pseudotuberculosis* mJΔyopM | YopM$^{PestA}$ Ala1 (N120A, Y135A, and N140A) | This study |
| pMMB67EH_YopM$^{PestA}$ Ala2 | *Y. pseudotuberculosis* mJΔyopM | YopM$^{PestA}$ (D159A, D161A, and F177A) | This study |
| pMMB67EH_YopM$^{PestA}$ D159A | *Y. pseudotuberculosis* mJΔyopM | YopM$^{PestA}$ (D159A) | This study |
| pMMB67EH_YopM$^{PestA}$ D161A | *Y. pseudotuberculosis* mJΔyopM | YopM$^{PestA}$ (D161A) | This study |
| pMMB67EH_YopM$^{PestA}$ F177A | *Y. pseudotuberculosis* mJΔyopM | YopM$^{PestA}$ (F177A) | This study |
| pMMB67EH_YopM$^{PestA}$ Ala3 | *Y. pseudotuberculosis* mJΔyopM | YopM$^{PestA}$ Ala3 (Y201A, N221A, and E279A) | This study |
| pMMB67EH_YopM$^{KIM}$ WT | *Y. pseudotuberculosis* mJΔyopM | Full-length YopM$^{KIM}$ CDS | This study |
| pMMB67EH_YopM$^{KIM}$ Ala2 | *Y. pseudotuberculosis* mJΔyopM | YopM $^{KIM}$ Ala2 (D159A, D161A, and F177A) | This study |

## References


1. G. R. Cornelis, F. Van Gijsegem, Assembly and function of type III secretory systems. *Annu. Rev. Microbiol.* **54**, 735-774 (2000).
2. J. E. Galan, A. Collmer, Type III secretion machines: bacterial devices for protein delivery into host cells. *Science* **284**, 1322-1328 (1999).
3. R. E. Vance, R. R. Isberg, D. A. Portnoy, Patterns of pathogenesis: discrimination of pathogenic and nonpathogenic microbes by the innate immune system. *Cell Host Microbe* **6**, 10-21 (2009).
4. S. Shin, I. E. Brodsky, The inflammasome: Learning from bacterial evasion strategies. *Semin Immunol* 10.1016/j.smim.2015.03.006 (2015).
5. S. B. Kovacs, E. A. Miao, Gasdermins: Effectors of Pyroptosis. *Trends Cell Biol* 10.1016/j.tcb.2017.05.005 (2017).
6. J. Shi, W. Gao, F. Shao, Pyroptosis: Gasdermin-Mediated Programmed Necrotic Cell Death. *Trends Biochem Sci* **42**, 245-254 (2017).

7. T. Bergsbaken, S. L. Fink, A. B. den Hartigh, W. P. Loomis, B. T. Cookson, Coordinated host responses during pyroptosis: caspase-1-dependent lysosome exocytosis and inflammatory cytokine maturation. *J Immunol* **187**, 2748-2754 (2011).
8. S. Ramos, E. Hartenian, P. Broz, Programmed cell death: NINJ1 and mechanisms of plasma membrane rupture. *Trends Biochem Sci* **49**, 717-728 (2024).
9. S. M. Brewer, S. W. Brubaker, D. M. Monack, Host inflammasome defense mechanisms and bacterial pathogen evasion strategies. *Curr Opin Immunol* **60**, 63-70 (2019).
10. K. M. Davis, All Yersinia Are Not Created Equal: Phenotypic Adaptation to Distinct Niches Within Mammalian Tissues. *Front Cell Infect Microbiol* **8**, 261 (2018).
11. J. B. Bliska, I. E. Brodsky, J. Mecsas, Role of the Yersinia pseudotuberculosis Virulence Plasmid in Pathogen-Phagocyte Interactions in Mesenteric Lymph Nodes. *EcoSal Plus* **9**, eESP00142021 (2021).
12. J. B. Bliska, X. Wang, G. I. Viboud, I. E. Brodsky, Modulation of innate immune responses by Yersinia type III secretion system translocators and effectors. *Cell Microbiol* **15**, 1622-1631 (2013).
13. D. S. Black, J. B. Bliska, The RhoGAP activity of the Yersinia pseudotuberculosis cytotoxin YopE is required for antiphagocytic function and virulence. *Mol Microbiol* **37**, 515-527 (2000).
14. F. Shao, J. E. Dixon, YopT is a cysteine protease cleaving Rho family GTPases. *Adv Exp Med Biol* **529**, 79-84 (2003).
15. L. K. Chung *et al.*, The Yersinia Virulence Factor YopM Hijacks Host Kinases to Inhibit Type III Effector-Triggered Activation of the Pyrin Inflammasome. *Cell Host Microbe* **20**, 296-306 (2016).
16. D. Ratner *et al.*, The Yersinia pestis Effector YopM Inhibits Pyrin Inflammasome Activation. *PLoS Pathog* **12**, e1006035 (2016).
17. K. W. Ma, W. Ma, YopJ Family Effectors Promote Bacterial Infection through a Unique Acetyltransferase Activity. *Microbiol Mol Biol Rev* **80**, 1011-1027 (2016).
18. L. E. Palmer, S. Hobbie, J. E. Galan, J. B. Bliska, YopJ of *Yersinia pseudotuberculosis* is required for the inhibition of macrophage TNF-alpha production and downregulation of the MAP kinases p38 and JNK. *Mol Microbiol* **27**, 953-965 (1998).
19. S. Mukherjee *et al.*, Yersinia YopJ acetylates and inhibits kinase activation by blocking phosphorylation. *Science* **312**, 1211-1214 (2006).
20. T. J. Schoberle, L. K. Chung, J. B. McPhee, B. Bogin, J. B. Bliska, Uncovering an Important Role for YopJ in the Inhibition of Caspase-1 in Activated Macrophages and Promoting Yersinia pseudotuberculosis Virulence. *Infect Immun* **84**, 1062-1072 (2016).
21. H. Xu *et al.*, Innate immune sensing of bacterial modifications of Rho GTPases by the Pyrin inflammasome. *Nature* **513**, 237-241 (2014).
22. H. S. Malik, J. B. Bliska, Guards and decoys: RIPoptosome and inflammasome pathway regulators of bacterial effector-triggered immunity. *PLoS Pathog* **21**, e1012884 (2025).
23. H. S. Malik, J. B. Bliska, The pyrin inflammasome and the Yersinia effector interaction. *Immunol Rev* **297**, 96-107 (2020).
24. N. P. Medici, M. Rashid, J. B. Bliska, Characterization of pyrin dephosphorylation and inflammasome activation in macrophages as triggered by the Yersinia effectors YopE and YopT. *Infect Immun* 10.1128/IAI.00822-18 (2019).
25. O. Schnappauf, J. J. Chae, D. L. Kastner, I. Aksentijevich, The Pyrin Inflammasome in Health and Disease. *Front Immunol* **10**, 1745 (2019).
26. N. A. Loeven, N. P. Medici, J. B. Bliska, The pyrin inflammasome in host-microbe interactions. *Curr Opin Microbiol* **54**, 77-86 (2020).
27. K. Ozato, D. M. Shin, T. H. Chang, H. C. Morse, 3rd, TRIM family proteins and their emerging roles in innate immunity. *Nat Rev Immunol* **8**, 849-860 (2008).

28. C. Weinert, D. Morger, A. Djekic, M. G. Grutter, P. R. Mittl, Crystal structure of TRIM20 C-terminal coiled-coil/B30.2 fragment: implications for the recognition of higher order oligomers. *Sci Rep* **5**, 10819 (2015).
29. B. K. Ganser-Pornillos, O. Pornillos, Restriction of HIV-1 and other retroviruses by TRIM5. *Nat Rev Microbiol* **17**, 546-556 (2019).
30. H. S. Malik *et al.*, Phosphoprotein phosphatase activity positively regulates oligomeric pyrin to trigger inflammasome assembly in phagocytes. *mBio* 10.1128/mbio.02066-23, e0206623 (2023).
31. J. W. Yu *et al.*, Pyrin activates the ASC pyroptosome in response to engagement by autoinflammatory PSTPIP1 mutants. *Mol Cell* **28**, 214-227 (2007).
32. W. Gao, J. Yang, W. Liu, Y. Wang, F. Shao, Site-specific phosphorylation and microtubule dynamics control Pyrin inflammasome activation. *Proc Natl Acad Sci U S A* **113**, E4857-4866 (2016).
33. Y. H. Park, G. Wood, D. L. Kastner, J. J. Chae, Pyrin inflammasome activation and RhoA signaling in the autoinflammatory diseases FMF and HIDS. *Nat Immunol* **17**, 914-921 (2016).
34. F. Magnotti *et al.*, Pyrin dephosphorylation is sufficient to trigger inflammasome activation in familial Mediterranean fever patients. *EMBO Mol Med* **11**, e10547 (2019).
35. F. Magnotti *et al.*, Steroid hormone catabolites activate the pyrin inflammasome through a non-canonical mechanism. *Cell Rep* **41**, 111472 (2022).
36. R. Lau, M. M. Hann, C. Ottmann, Crystal structure and ligandability of the 14-3-3/pyrin interface. *Biochem Biophys Res Commun* **651**, 1-7 (2023).
37. C. McDonald, P. O. Vacratsis, J. B. Bliska, J. E. Dixon, The Yersinia virulence factor YopM forms a novel protein complex with two cellular kinases. *J Biol Chem* **278**, 18514-18523 (2003).
38. M. Hentschke *et al.*, Yersinia virulence factor YopM induces sustained RSK activation by interfering with dephosphorylation. *PLoS One* **5**, e13165 (2010).
39. Y. H. Park *et al.*, Ancient familial Mediterranean fever mutations in human pyrin and resistance to Yersinia pestis. *Nat Immunol* 10.1038/s41590-020-0705-6 (2020).
40. J. B. McPhee, P. Mena, J. B. Bliska, Delineation of regions of the Yersinia YopM protein required for interaction with the RSK1 and PRK2 host kinases and their requirement for interleukin-10 production and virulence. *Infect Immun* **78**, 3529-3539 (2010).
41. M. W. McCoy, M. L. Marre, C. F. Lesser, J. Mecsas, The C-terminal tail of Yersinia pseudotuberculosis YopM is critical for interacting with RSK1 and for virulence. *Infect Immun* **78**, 2584-2598 (2010).
42. S. Norkowski, M. A. Schmidt, C. Ruter, The species-spanning family of LPX-motif harbouring effector proteins. *Cell Microbiol* **20**, e12945 (2018).
43. A. G. Evdokimov, D. E. Anderson, K. M. Routzahn, D. S. Waugh, Unusual molecular architecture of the Yersinia pestis cytotoxin YopM: a leucine-rich repeat protein with the shortest repeating unit. *J Mol Biol* **312**, 807-821 (2001).
44. A. Boland *et al.*, Status of YopM and YopN in the *Yersinia* Yop virulon: YopM of *Y. enterocolitica* is internalized inside the cytosol of PU5-1.8 macrophages by the YopB, D, N delivery apparatus. *EMBO J.* **15**, 5191-5201 (1996).
45. A. Alexa *et al.*, A non-catalytic herpesviral protein reconfigures ERK-RSK signaling by targeting kinase docking systems in the host. *Nat Commun* **13**, 472 (2022).
46. M. Achtman *et al.*, Microevolution and history of the plague bacillus, Yersinia pestis. *Proc Natl Acad Sci U S A* **101**, 17837-17842 (2004).
47. L. Berneking *et al.*, Immunosuppressive Yersinia Effector YopM Binds DEAD Box Helicase DDX3 to Control Ribosomal S6 Kinase in the Nucleus of Host Cells. *PLoS Pathog* **12**, e1005660 (2016).

48. J. Wen, T. Arakawa, J. S. Philo, Size-exclusion chromatography with on-line light-scattering, absorbance, and refractive index detectors for studying proteins and their interactions. *Anal Biochem* **240**, 155-166 (1996).
49. D. Some, H. Amartely, A. Tsadok, M. Lebendiker, Characterization of Proteins by Size-Exclusion Chromatography Coupled to Multi-Angle Light Scattering (SEC-MALS). *J Vis Exp* 10.3791/59615 (2019).
50. J. Ding *et al.*, Structural and Functional Insights into Host Death Domains Inactivation by the Bacterial Arginine GlcNAcyltransferase Effector. *Mol Cell* **74**, 922-935 e926 (2019).
51. Y. S. Huoh, S. Hur, Death domain fold proteins in immune signaling and transcriptional regulation. *FEBS J* **289**, 4082-4097 (2022).
52. D. Eliezer, Folding pyrin into the family. *Structure* **11**, 1190-1191 (2003).
53. P. R. Vajjhala *et al.*, Identification of multifaceted binding modes for pyrin and ASC pyrin domains gives insights into pyrin inflammasome assembly. *J Biol Chem* **289**, 23504-23519 (2014).
54. P. R. Vajjhala, R. E. Mirams, J. M. Hill, Multiple binding sites on the pyrin domain of ASC protein allow self-association and interaction with NLRP3 protein. *J Biol Chem* **287**, 41732-41743 (2012).
55. J. W. Yu *et al.*, Cryopyrin and pyrin activate caspase-1, but not NF-kappaB, via ASC oligomerization. *Cell Death Differ* **13**, 236-249 (2006).
56. I. Touitou *et al.*, Infevers: an evolving mutation database for auto-inflammatory syndromes. *Hum Mutat* **24**, 194-198 (2004).
57. M. D. Daugherty, H. S. Malik, Rules of engagement: molecular insights from host-virus arms races. *Annu Rev Genet* **46**, 677-700 (2012).
58. A. Battesti, E. Bouveret, The bacterial two-hybrid system based on adenylate cyclase reconstitution in Escherichia coli. *Methods* **58**, 325-334 (2012).
59. G. Karimova, J. Pidoux, A. Ullmann, D. Ladant, A bacterial two-hybrid system based on a reconstituted signal transduction pathway. *Proc Natl Acad Sci U S A* **95**, 5752-5756 (1998).
60. J. Dam, P. Schuck, Calculating sedimentation coefficient distributions by direct modeling of sedimentation velocity concentration profiles. *Methods Enzymol* **384**, 185-212 (2004).
61. N. Nayeem, Y. Zhang, D. K. Schweppe, D. R. Madden, T. Green, A nondesensitizing kainate receptor point mutant. *Mol Pharmacol* **76**, 534-542 (2009).
62. W. Kabsch, Integration, scaling, space-group assignment and post-refinement. *Acta Crystallogr D Biol Crystallogr* **66**, 133-144 (2010).
63. D. Liebschner *et al.*, Macromolecular structure determination using X-rays, neutrons and electrons: recent developments in Phenix. *Acta Crystallogr D Struct Biol* **75**, 861-877 (2019).
64. P. Emsley, B. Lohkamp, W. G. Scott, K. Cowtan, Features and development of Coot. *Acta Crystallogr D Biol Crystallogr* **66**, 486-501 (2010).
65. B. W. Matthews, Solvent content of protein crystals. *J Mol Biol* **33**, 491-497 (1968).
66. H. M. Berman *et al.*, The Protein Data Bank. *Nucleic Acids Res* **28**, 235-242 (2000).
67. L. Schrödinger, The PyMOL Molecular Graphics System, Version 3.0.0. (2010).
68. J. Agirre *et al.*, The CCP4 suite: integrative software for macromolecular crystallography. *Acta Crystallogr D Struct Biol* **79**, 449-461 (2023).
69. C. Herre *et al.*, Introduction of the Capsules environment to support further growth of the SBGrid structural biology software collection. *Acta Crystallogr D Struct Biol* **80**, 439-450 (2024).
70. E. Jurrus *et al.*, Improvements to the APBS biomolecular solvation software suite. *Protein Sci* **27**, 112-128 (2018).
71. R. C. Team, R: A Language and Environment for Statistical
72. H. Wickham *et al.*, Welcome to the tidyverse. *Journal of Open Source Software* **4, 1686.** (2019).

911 73. C. Dawson, ggprism: A ‘ggplot2’ Extension Inspired by ‘GraphPad Prism’. R package version
912 1.0.7. doi: 10.5281/zenodo.4556067 (2025).
913 74. C. Dawson, ggprism: A 'ggplot2' Extension Inspired by 'GraphPad Prism'. (2022).
914 75. N. P. Medici, J. B. Bliska, Methods for Detection of Pyrin Inflammasome Assembly in
915 Macrophages Infected with Yersinia spp. *Methods Mol Biol* **2010**, 241-255 (2019).
916 76. K. Diederichs, P. A. Karplus, Improved R-factors for diffraction data analysis in
917 macromolecular crystallography. *Nat Struct Biol* **4**, 269-275 (1997).
918 77. P. A. Karplus, K. Diederichs, Linking crystallographic model and data quality. *Science* **336**,
919 1030-1033 (2012).

920

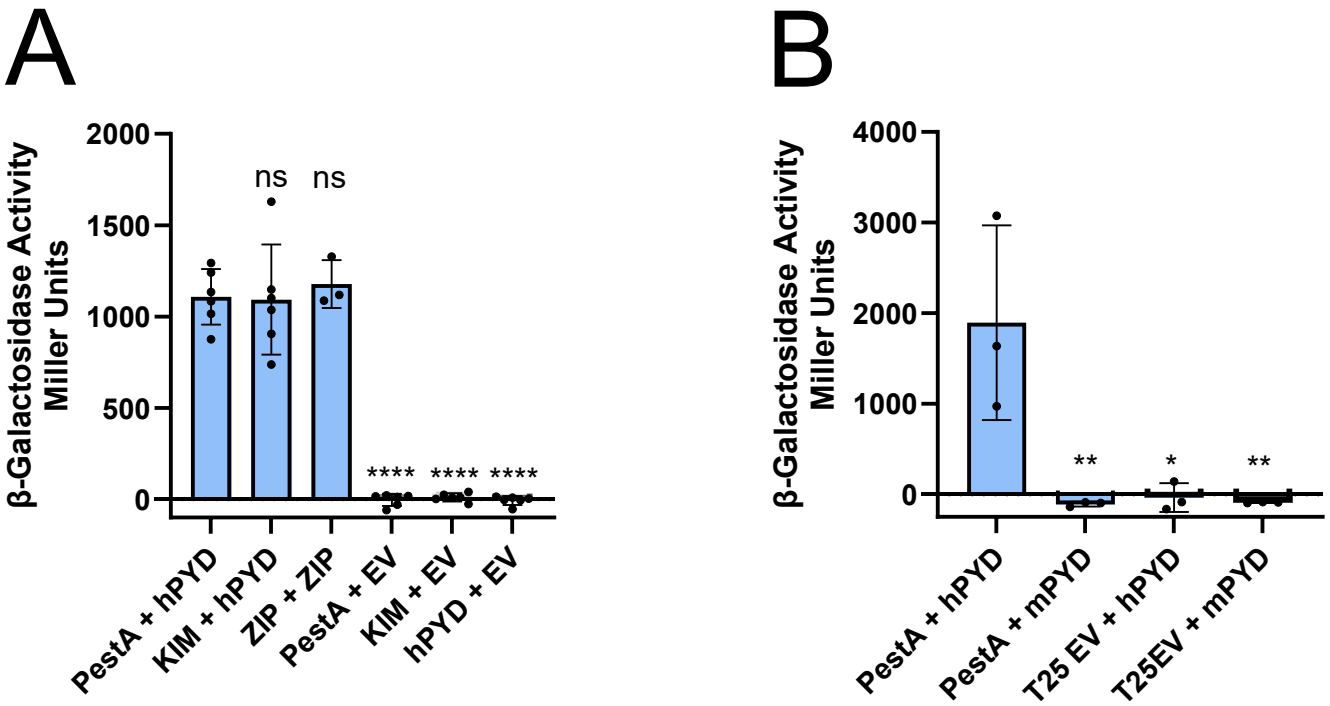


**Fig. 1. Analysis of YopM-PYD interactions using BACTH.** The indicated YopM proteins were N-terminally tagged with T25 and hPYDs (**A, B**) or mPYDs (**B**) were C-terminally tagged with T18. Plasmids encoding the fused partners, ZIP positive controls or empty vector (EV) controls were co-transformed into *E. coli* to test for protein-protein interactions. Measured Miller units of β-galactosidase activity indicating protein interaction in *E. coli* are indicated on the y-axis. Results are averages and standard deviations with data pooled from at least 3 independent experiments. Significance determined by one-way ANOVA and Tukey's post hoc test in comparison to PestA + hPYD.**** $p<0.0001$, ** $p=0.0085$ (PestA + mPYD) and 0.0090 (T25EV + mPYD), * $p=0.0105$ ns, not significant.

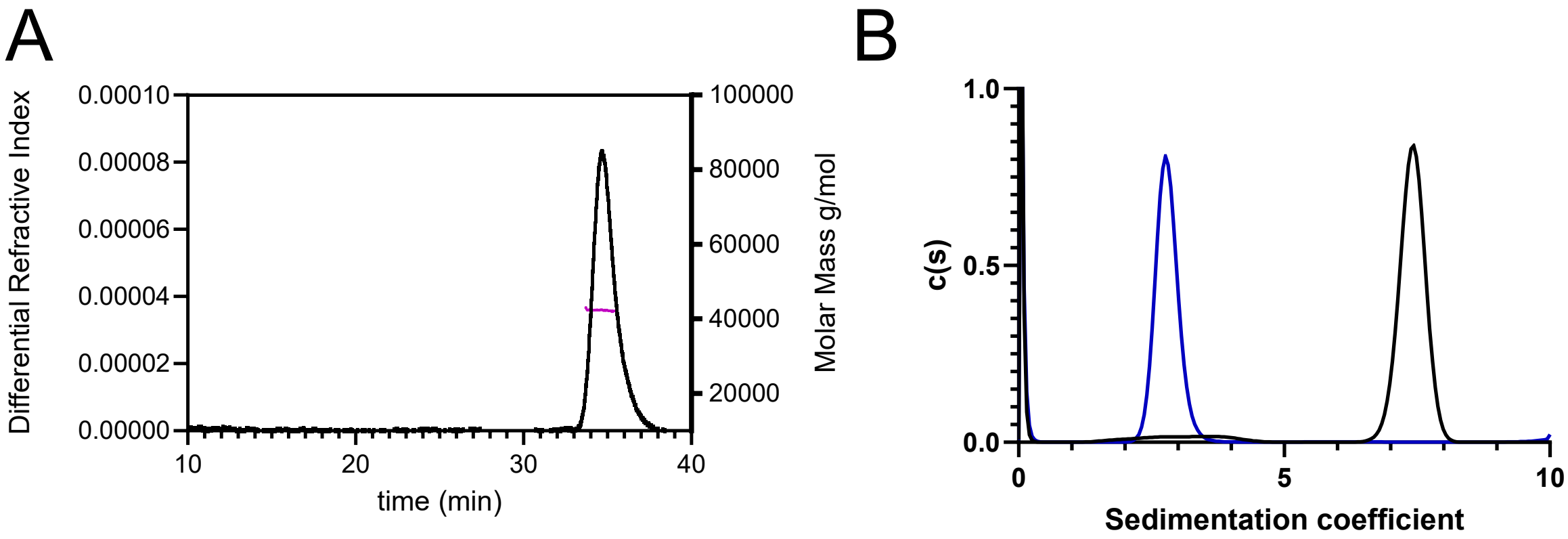


**Fig. 2. Characterization of YopM$^{PestA}$ in solution by SEC-MALs or vAUC. A)** SEC-MALS analysis of YopM$^{PestA}$ at pH 7.4. The experimental relative molar mass across the peak width is plotted in magenta (right-hand axis), overlaid with the differential refractive index (left-hand axis) of the chromatogram. The estimated relative molar mass is 42.9 kDa. **B)** Sedimentation coefficient distribution of YopM$^{PestA}$ by vAUC at pH 7.4 (Blue; main peak, corresponding to an estimated $M_r$ of 43.5 kDa) and pH 5.0 (Black; main peak, corresponding to an estimated $M_r$ of 148.2kDa).

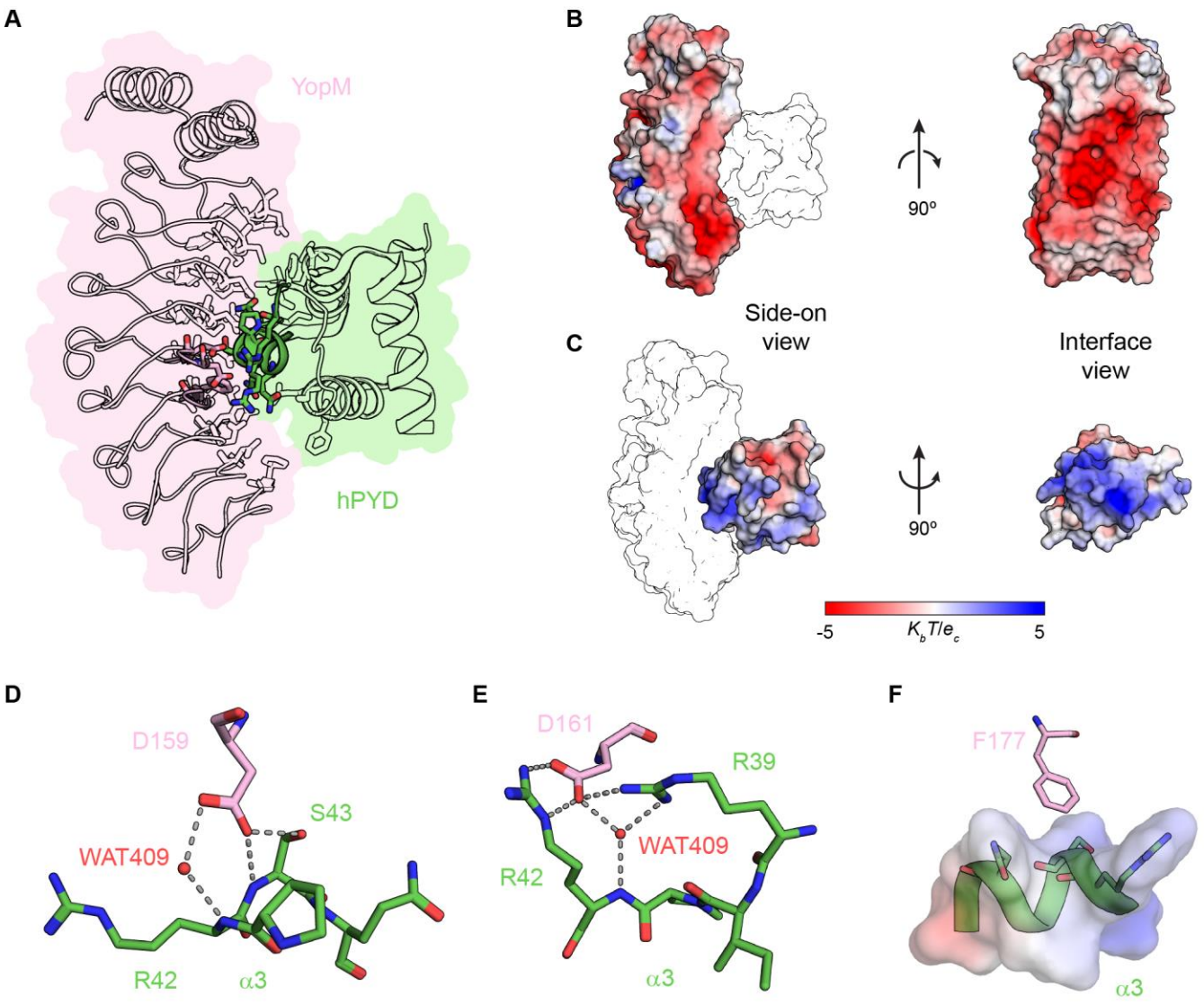


**Fig. 3. hPYD binds to the concave surface of YopM.** The co-crystal structure of YopM$^{PestA*}$-hPYD* reveals a binding interface composed of the negatively charged concave surface of YopM spanning LRRs 1-9 and the positively charged surface of hPYD involving α-helices 2-4. **A)** YopM (pink) and hPYD (green) are depicted as ribbon outlines, with interfacial residues depicted as stick outlines. The YopM residues selected for mutation (YopM Ala2) and cognate hPYD residues are highlighted as pink and green sticks, respectively. **B and C)** The electrostatic surfaces of YopM (**B**) and hPYD (**C**) are shown in orthogonal views. As a visual aid, the second protein of the complex is shown as a black-and-white outline in the side-on view (left-hand panel). **D-F)** Focused views of interactions highlighted in (A) between YopM and hPYD helix α3 that are disrupted in the YopM Ala2 mutant. YopM D159 (**D**) and D161 (**E**) are the foci of hydrogen-bond networks with hPYD α3 that involve structural water WAT409 and salt-bridges with hPYD R39 and R42. YopM F177 (**F**) packs against hPYD α3, becoming shielded from solvent by apolar and polar atoms of hPYD. Non-carbon atoms are colored by type: oxygen, red; nitrogen, blue.

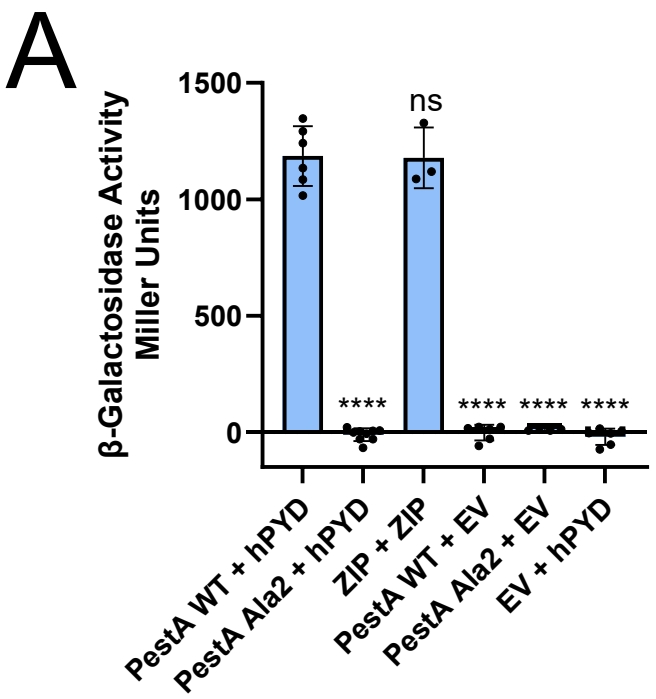


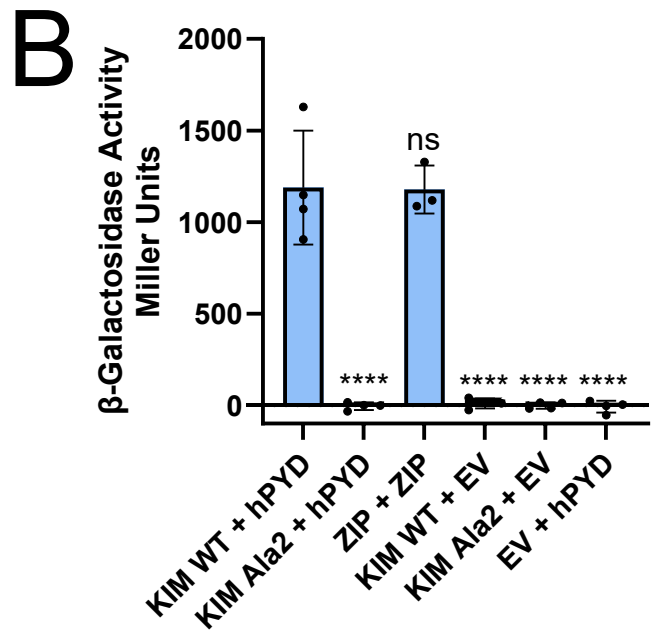


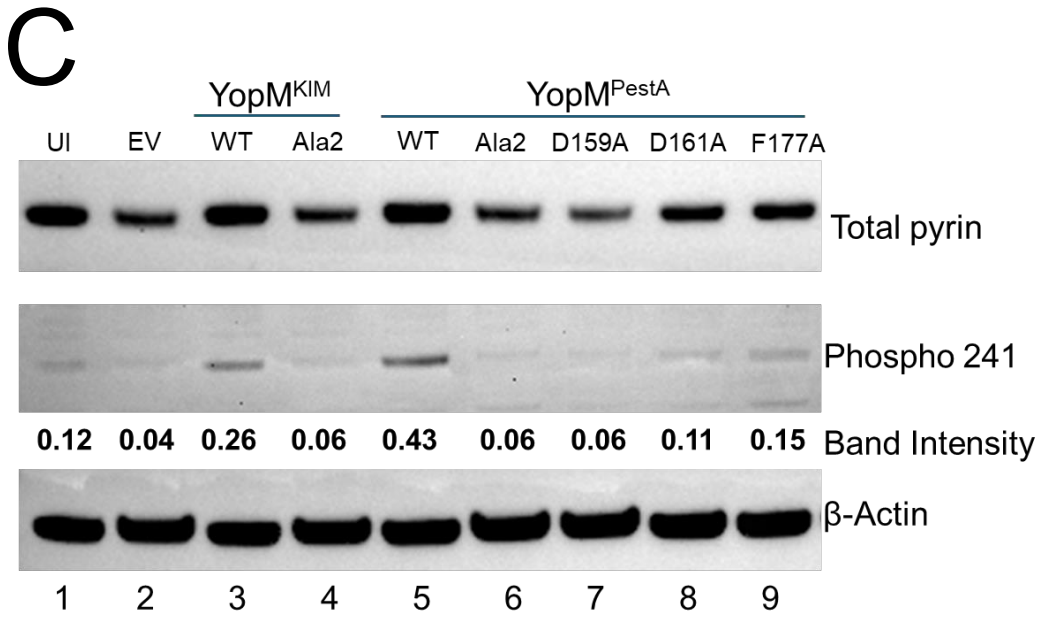


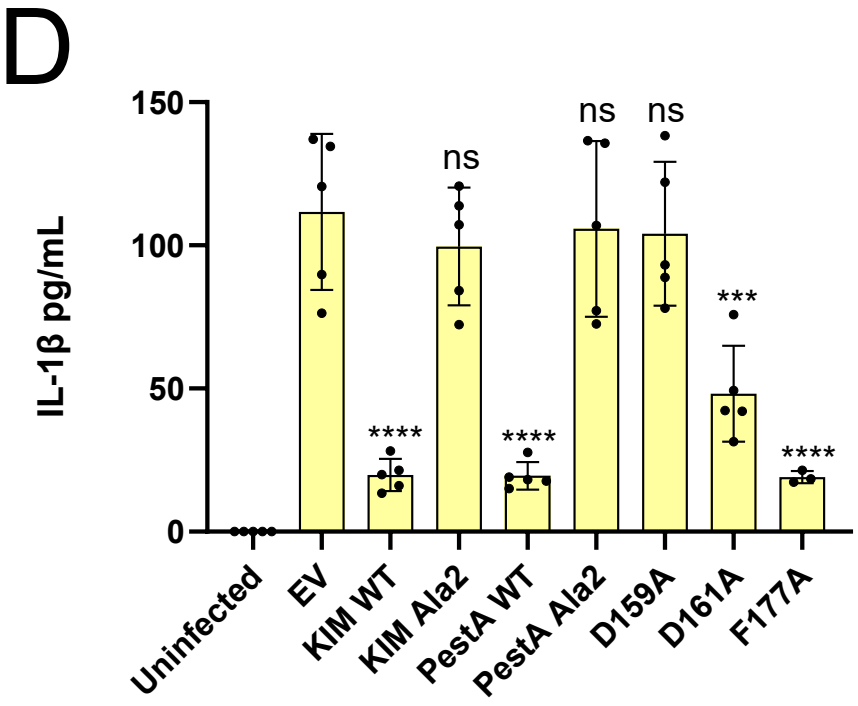


**Fig. 4. Analysis of YopM variants by BACTH or THP-1 infection assays. A,B)** The indicated YopM proteins were N-terminally tagged with T25, and hPYDs were C-terminally tagged with T18. Plasmids encoding the fused partners, ZIP positive controls or empty vector (EV) controls were co-transformed into *E. coli* to test for BACTH interactions as in Fig.1. Significance determined by one-way ANOVA and Tukey's *post hoc* test in comparison to PestA (**A**) or KIM (**B**) with hPYD. **C,D)** THP-1 cells were left uninfected (UI) or infected for 4 h at MOI 30 with *Y. pseudotuberculosis yopJ*$^{C172A}$Δ*yopM* complemented with empty vector (EV) or the indicated YopM isoforms or variants. **C)** Immunoblot analysis of THP-1 lysates with the indicated antibodies. Band intensity signals show the ratio of phospho 241/total pyrin. Results are representative of two independent experiments. **D)** ELISA of IL-1β released from THP-1 cells. Results are averages and standard deviations with data pooled from at least 3 independent experiments. Significance determined by one-way ANOVA and Tukey's *post hoc* test. Comparisons of each group to EV are shown. ****$p<0.0001$; ***$p<0.001$; ns, not significant.

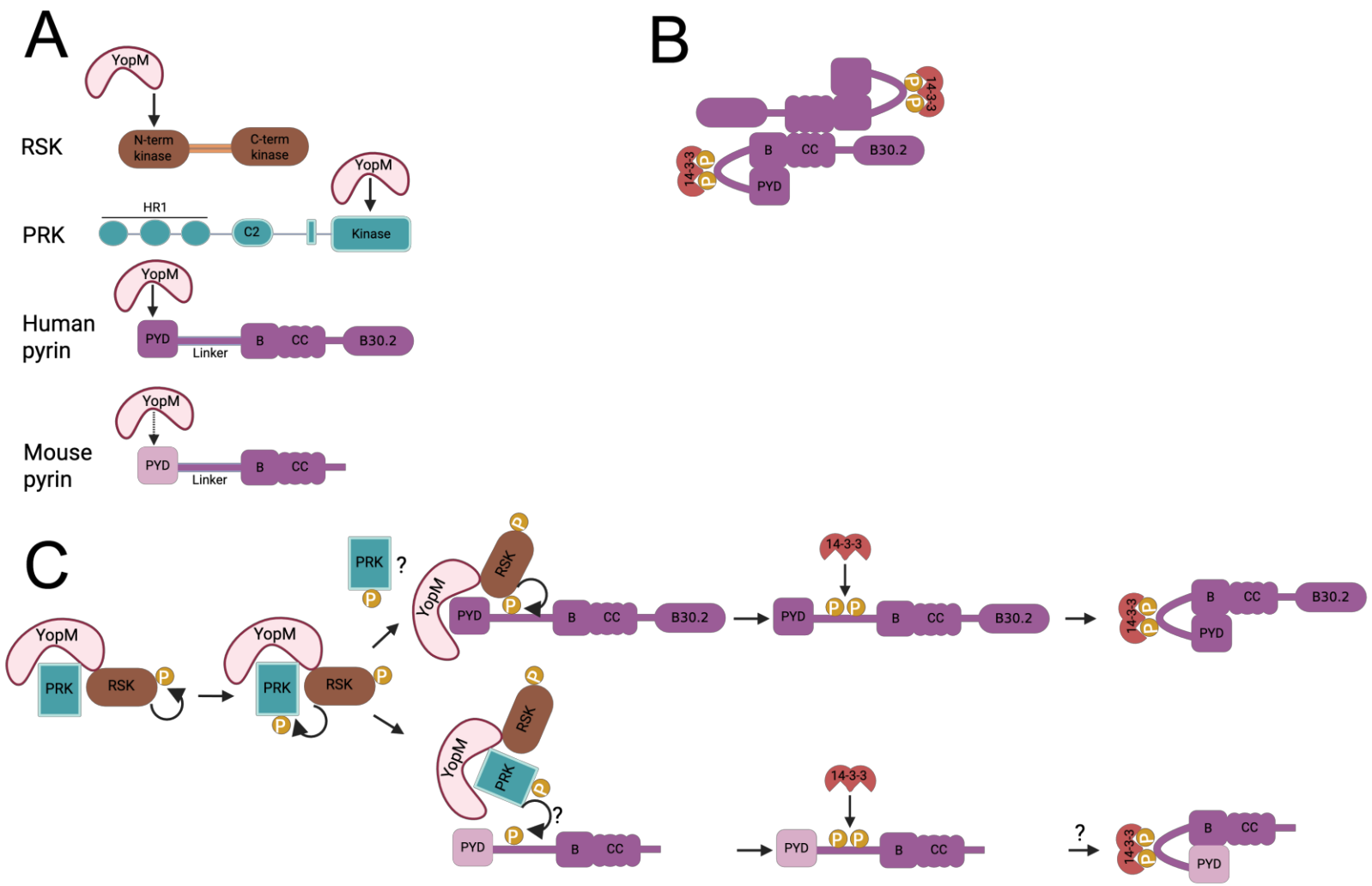


**Fig.S1. Scheme depicting YopM binding partners and mechanisms of pyrin targeting and inactivation. A)** Domain arrangements of RSK, PRK, and monomeric human and mouse pyrin and regions targeted for binding by YopM. The C-terminus of YopM binds the N-terminal kinase domain of RSK, and the concave surface of YopM LRR domain binds the kinase domain of PRK and the PYDs of human and mouse pyrin, the latter weakly (dashed arrow). Color shading is used to denote amino acid sequence difference between human and murine PYDs. HR1=homology region 1; C2=C2-like domain; B=B-box; CC=coiled coil. **B)** Anti-parallel dimer of inactive pyrin resulting from coiled-coil interactions. **C.** Model of YopM hijacking and sequentially activating by phosphorylation RSK and PRK and different targeting mechanisms for human and mouse pyrin. Individual kinase domains of RSK and PRK and monomeric pyrin proteins are shown for simplicity. Phosphorylation of two serine residues in the pyrin linker results in binding of a 14-3-3 dimer and the formation of a hairpin that facilitates sequestration of the PYD by the B-box. To inactivate human pyrin YopM releases PRK prior to PYD binding and using hijacked RSK to phosphorylate the linker. Role of the released PRK is unknown. To inactivate mouse pyrin YopM uses hijacked PRK to target and phosphorylate the linker. Role of the B-box in negative regulation of mouse pyrin is unknown.

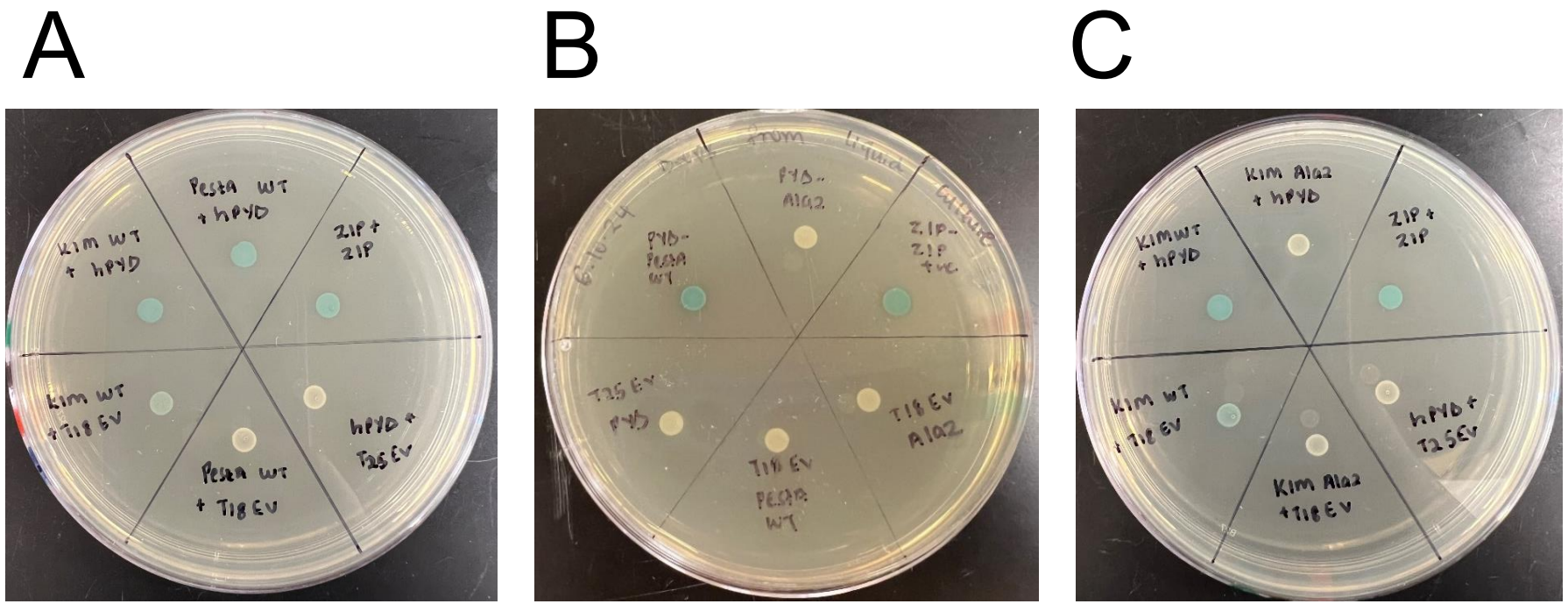


**Fig. S2. Analysis of YopM-PYD interactions using BACTH.** The indicated YopM proteins were N-terminally tagged with T25 and PYDs were C-terminally tagged with T18. Plasmids encoding the fused partners, ZIP positive controls or empty vector (T25 or T18 EV) controls were co-transformed into the *ΔcyaA E. coli* strain BTH101 to test for protein-protein interactions. Suspensions of colonies used for the β-galactosidase assays in Fig.1A (**A**), Fig. 4A (**B**) or Fig.4B (**C**) were dropped on a plate containing X-Gal for qualitative assessment of the protein interactions. Blue color indicates strong interactions and white color depicts weak interactions.

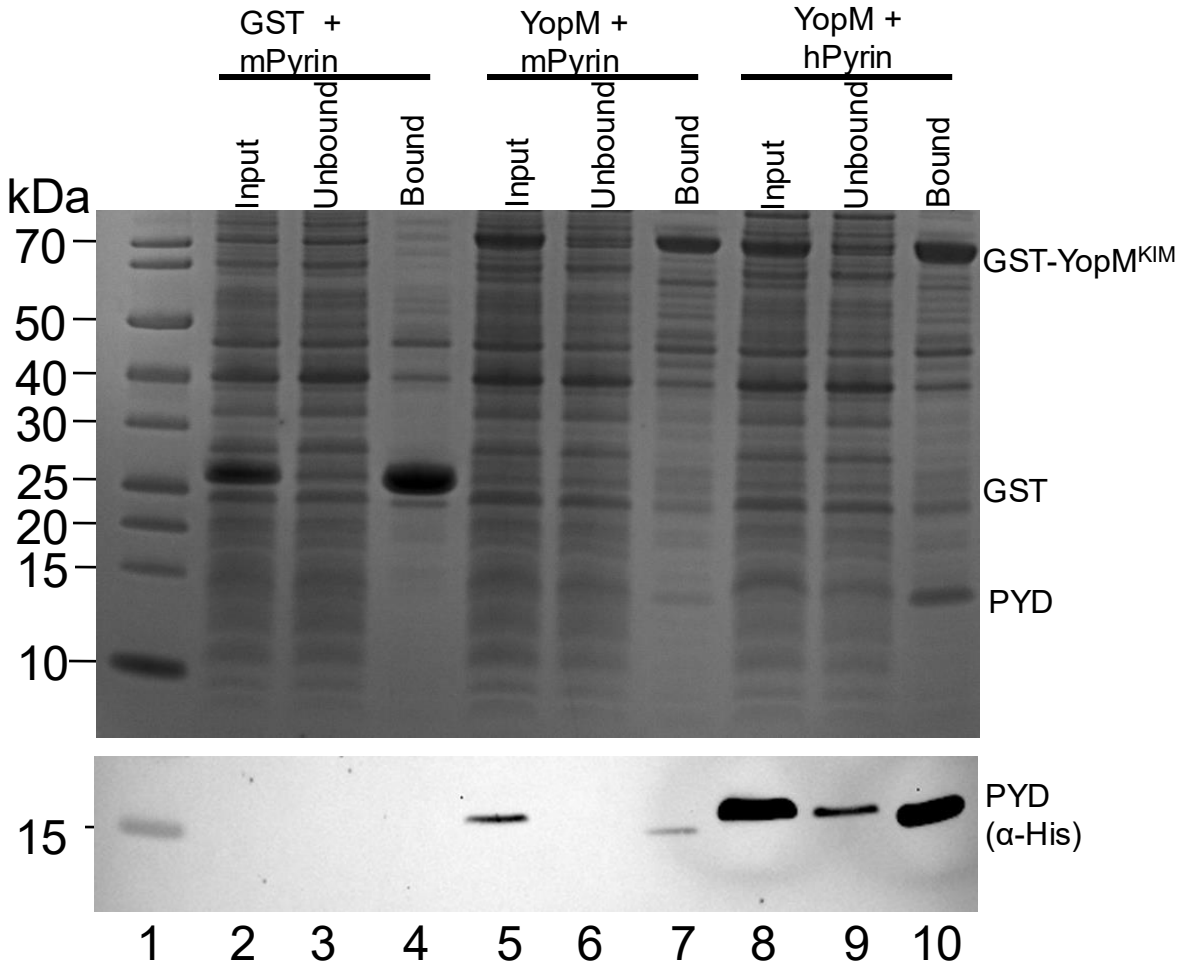


**Fig. S3. Analysis of YopM-PYD interactions by GST pulldown assay.** GST or GST-YopM$^{KIM}$ were co-expressed with His-tagged mPYD or hPYD in *E. coli* and the bacterial lysates were subjected to pull downs using GST resin. Samples of the input, unbound and bound fractions were analyzed by SDS-PAGE and blue protein staining (top) or $\alpha$-His immunoblotting (bottom). Lane 1 is a $M_r$ ladder with sizes labelled on the left. Positions of GST-YopM$^{KIM}$, GST, and PYDs are shown on the right.

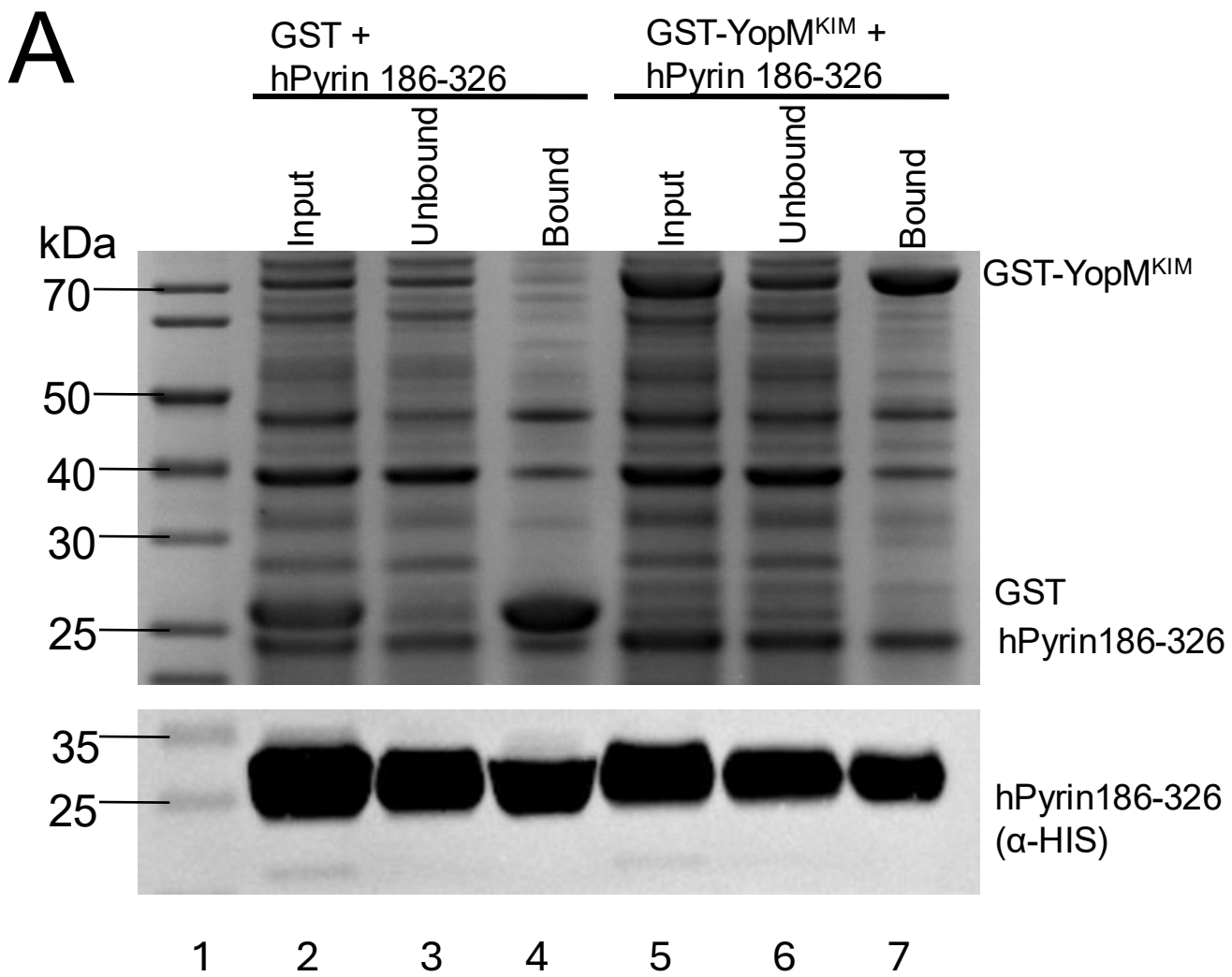


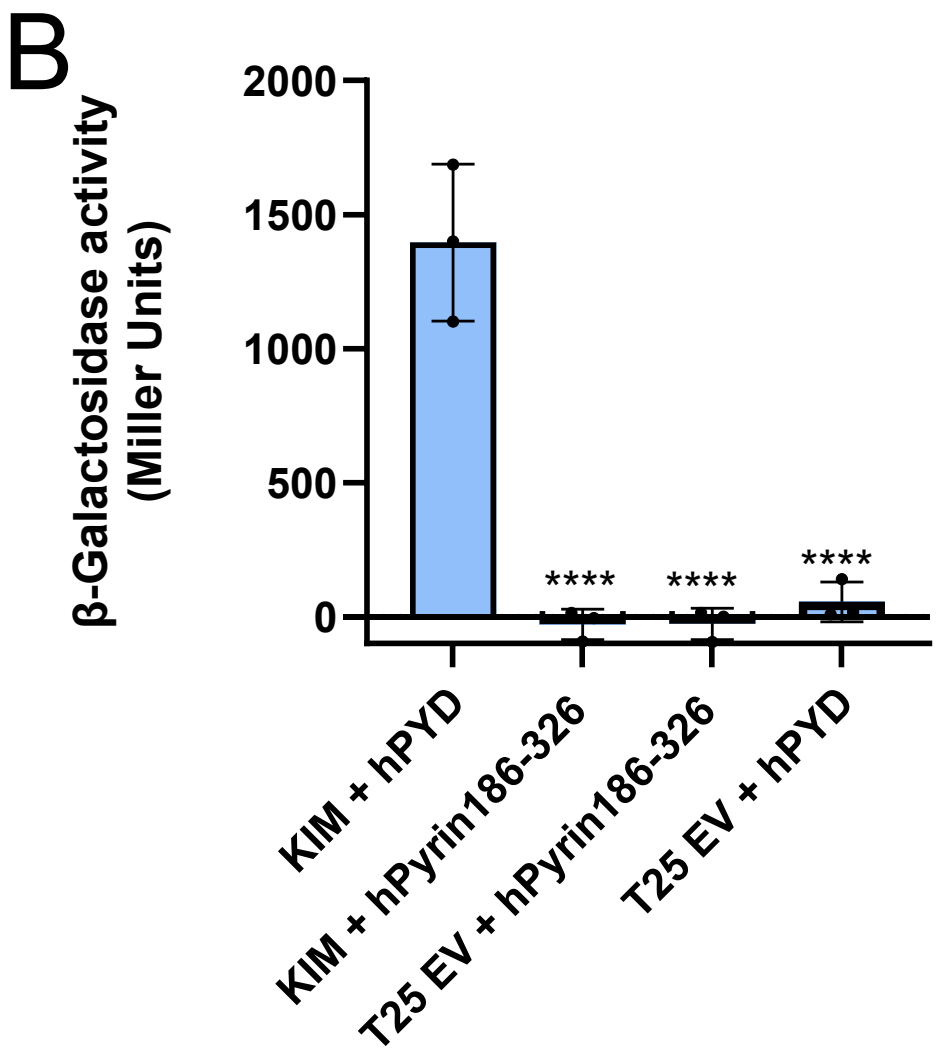


**Fig. S4. Analysis of YopM-pyrin linker interactions by GST pulldown or BACTH. A)** GST or GST-YopM$^{KIM}$ were co-expressed with His-tagged hPyrin186-326 in *E. coli* and the bacterial lysates were subjected to pull downs as in Fig. S3. **B)** BACTH analysis of YopM-hPyrin186-326 interactions. YopM$^{KIM}$ was N-terminally tagged with T25 and hPYD or hPyrin186-326 were C-terminally tagged with T18. Plasmids with the fused partners or empty vector (EV) controls were co-transformed into *E. coli* to test for protein-protein interactions as in Fig.1. Results are pooled from at least three independent experiments. Significance determined by one-way ANOVA and Tukey's post hoc test comparing to KIM + hPYD; **** $p<0.0001$.

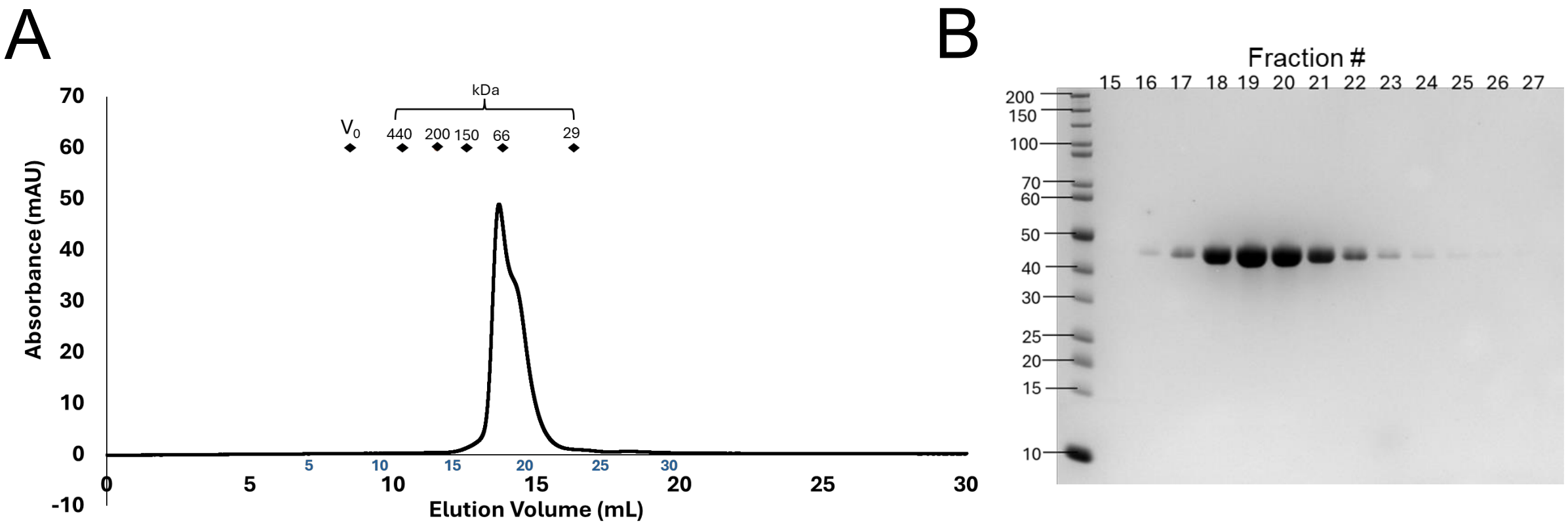


**Fig. S5. Characterization of YopM$^{PestA}$ by SEC.** YopM$^{PestA}$ was analyzed by SEC on a Superdex 200 10/300 column at 0.75 mL/min. Samples were analyzed in buffer containing 20 mM HEPES, 150 mM NaCl and 1 mM TCEP, pH 7.4. **A)** SEC chromatogram with fraction numbers shown in blue on the chromatograms above the elution volumes. Diamonds indicate the column void volume ($V_0$) and peak elution volumes of molecular mass standards (440 kDa = apoferritin, 200 kDa = β-amylase, 150 kDa = alcohol dehydrogenase, 66 kDa = albumin, 29 kDa = carbonic anhydrase). **B)** Fractions of the peak eluates were analyzed by SDS-PAGE and blue protein staining.

A

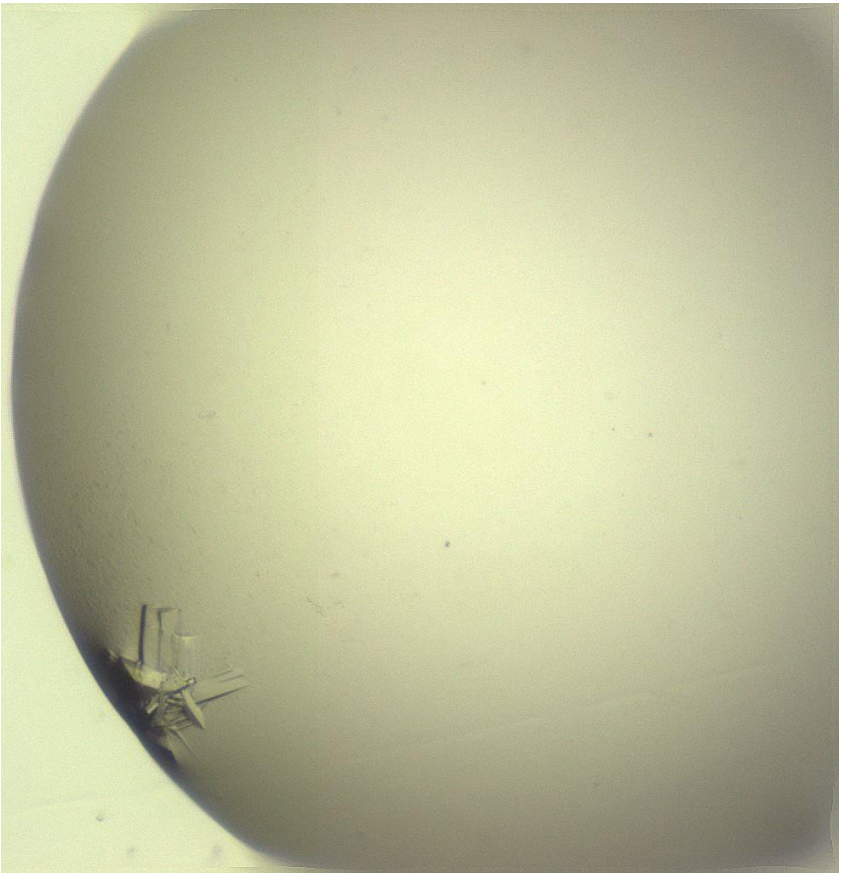

B

**Fig. S6. Representative images of YopM-hPYD complex crystals**. **A)** YopM$^{PestA}$ + hPYD crystals in 12% PEG 4K,0. MES, pH5.0 growing in sitting drops**. B)** YopM$^{\Delta N \Delta C}$ + hPYD crystals in 19% PEG 3350, 0.3 M NaSCN, 0.1 M Bis-Tris propane, pH 6.5 growing in hanging drops.

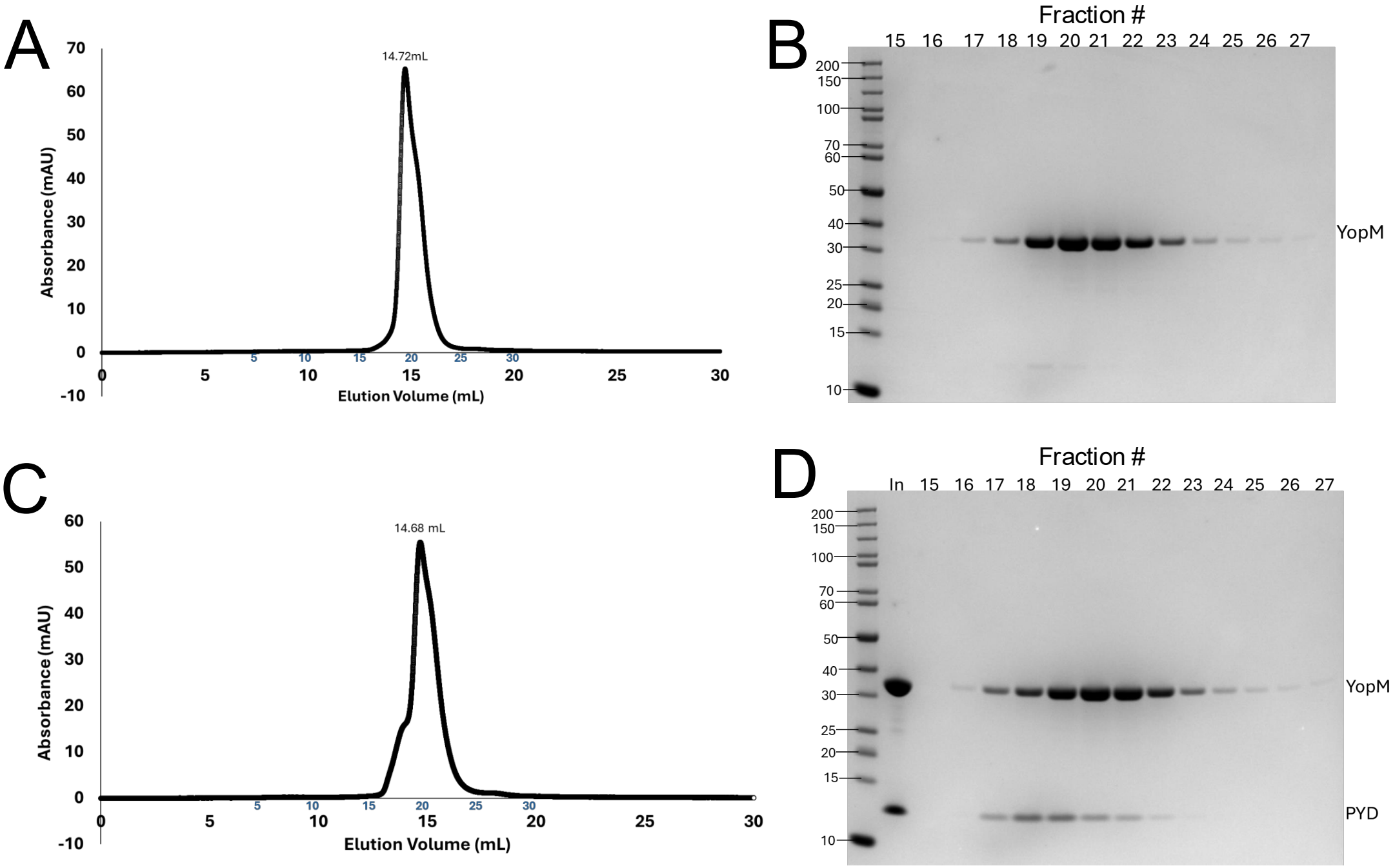


**Fig. S7. Characterization of YopM$^{\Delta N \Delta C}$ and the YopM$^{\Delta N \Delta C}$-hPYD complex by SEC.** YopM$^{\Delta N \Delta C}$ (**A,B**) or a 1:1 molar mixture of YopM$^{\Delta N \Delta C}$ and hPYD (**C,D**) were analyzed by SEC on a Superdex 200 10/300 column at 0.75 mL/min. Samples were analyzed in a buffer containing 20 mM HEPES, 150 mM NaCl and 1 mM TCEP, pH 7.4. **A,C)** SEC chromatograms, with fractions number in blue above elution volume. **B,D)** Fractions of the peak elutions were analyzed by SDS-PAGE and blue protein staining.

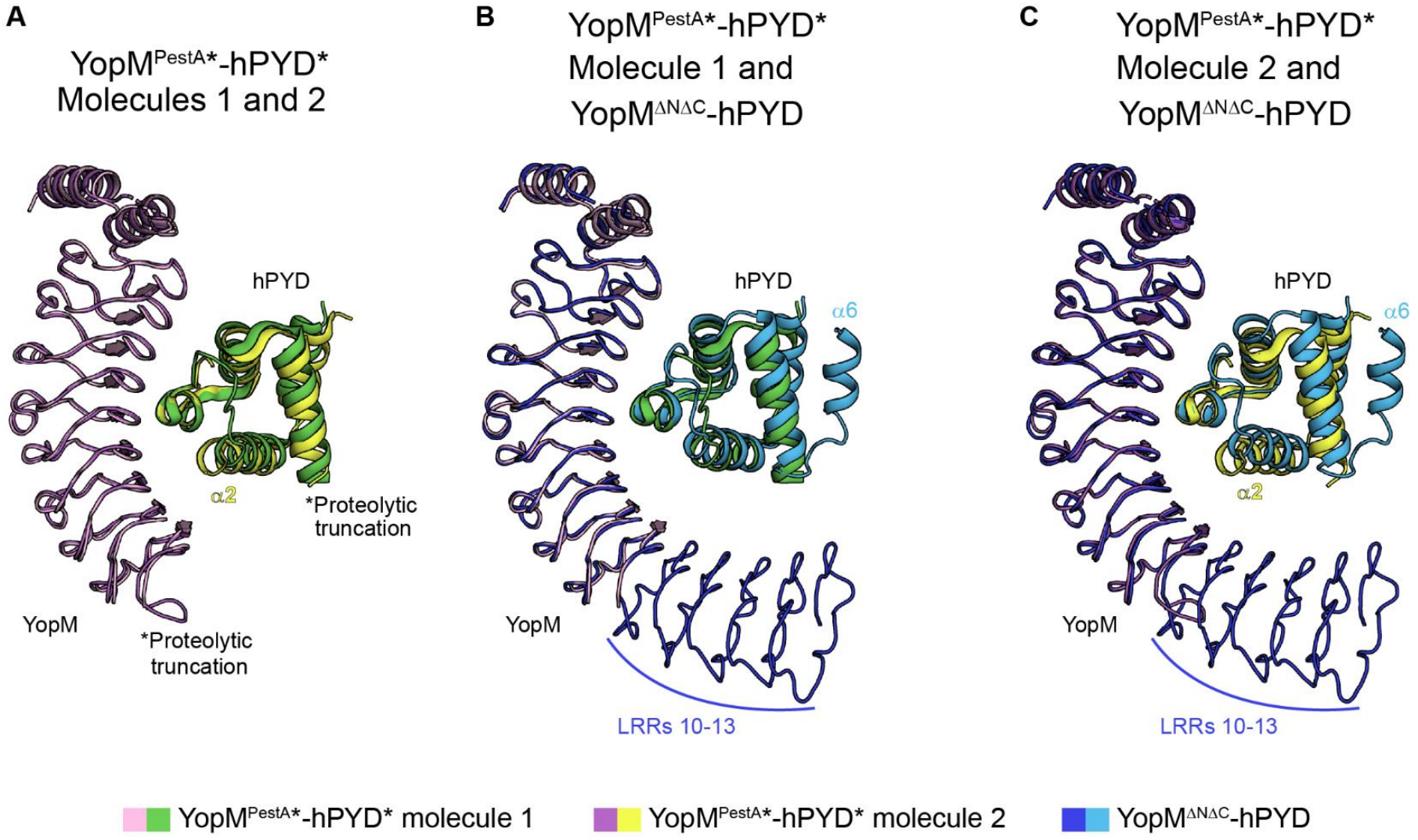


**Fig. S8. Heterogeneity in hPYD a2 is revealed by alignment of YopM$^{PestA}$-hPYD complexes.** The complexes of YopM$^{PestA}$ (pink, deep purple, and dark blue) and hPYD (green, yellow, and light blue) were aligned by all $C_a$ carbons in YopM$^{PestA}$, and key structural differences are labeled. **A)** Alignment of both molecules in the ASU of the limited proteolysis structure (YopM$^{PestA}$*-hPYD*) reveal differences in the position of hPYD a2 where one molecule makes additional interactions with the concave surface of YopM$^{PestA}$. **B and C)** Additional alignments of each molecule in (A) to a second co-crystal structure of YopM$^{DNDC}$-hPYD where all YopM LRRs and hPYD a-helices were resolved. The positioning of hPYD a2 is consistent between YopM$^{PestA}$*-hPYD* molecule 1 and YopM$^{DNDC}$-hPYD, as shown in (B).

A

```
MFINPRNVSNTFLQEPLRHSSNLTEMPVEAENVKSKTEYYNAWSEWERNAPPGNGEQREMAVSRLRDCLDRQAHELELNNLGLSSLPELPPHLES
1         10        20        30        40        50        60        70        80        90

LVASCNSLTELPELPQSLKSLLVDNNNLKALSDLPPLLEYLGVSNNQLEKLPELQNSSFLKIIDVDNNSLKKLPDLPPSLEFIAAGNNQLEELPE
   100       110       120       130       140       150       160       170       180       190

LQNLPFLTTIYADNNLLKTLPDLPPSLEALNVRDNYLTDLPELPQSLTFLDVSENIFSGLSELPPNLYYLNASSNEIRSLCDLPPSLEELNVSNN
        200       210       220       230       240       250       260       270       280

KLIELPALPPRLERLIASFNHLAEVPELPQNLKQLHVEYNPLREFPDIPESVEDLRMNSERVVDPYEFAHETTDKLEDDVFE
   290       300       310       320       330       340       350       360       367
```

- Ala1: N120A,Y135A&N140A
- Ala2: D159A,D161A&F177A
- Ala3: Y201A,N221A &E279A

B

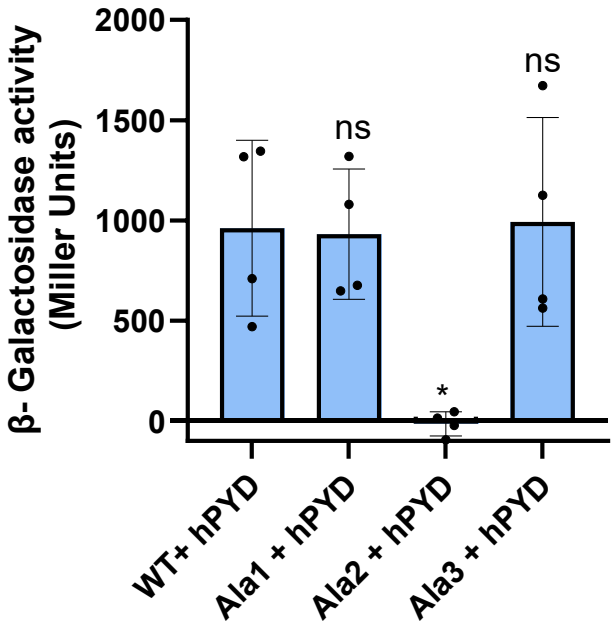


**Fig. S9. Identification by Ala substitution of amino acids in YopM$^{PestA}$ that are important for hPYD binding. A)** Amino acid sequence of YopM$^{PestA}$ highlighting residues in the three-series alanine substitution variants by color: Ala1 (blue), Ala2 (red) and Ala3 (orange). **B)** Analysis of YopM$^{PestA}$ Ala variants binding to hPYD using BACTH. Plasmids with the indicated fused partners were co-transformed into *E. coli* to test for protein-protein interactions as in Fig.1. Results are pooled from three independent experiments. Significance determined by one-way ANOVA and Tukey's post hoc test comparing to PestA + hPYD; * p=0.0154, ns not significant.

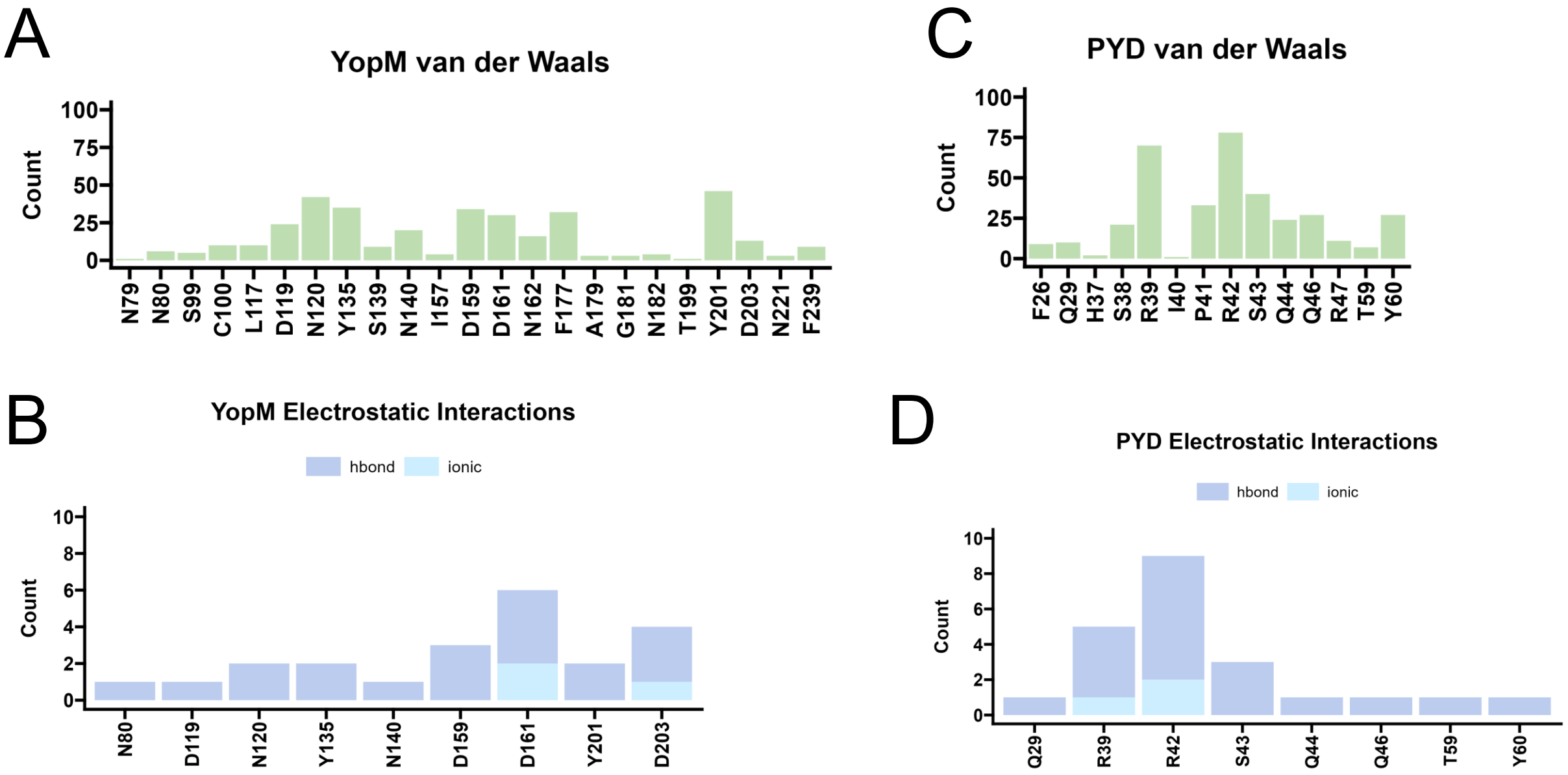


**Fig. S10. Residues contributing to the binding interface of YopM$^{PestA}$-hPYD.** The frequency with which each residue makes an interaction is plotted as counts on the y-axis. The y-axis denotes the residue position for the indicated protein**. A,B)** Plot of Van der Waals interactions. **C,D.** Plot of electrostatic interactions showing hydrogen bonds in dark blue and ionic charges in light blue.

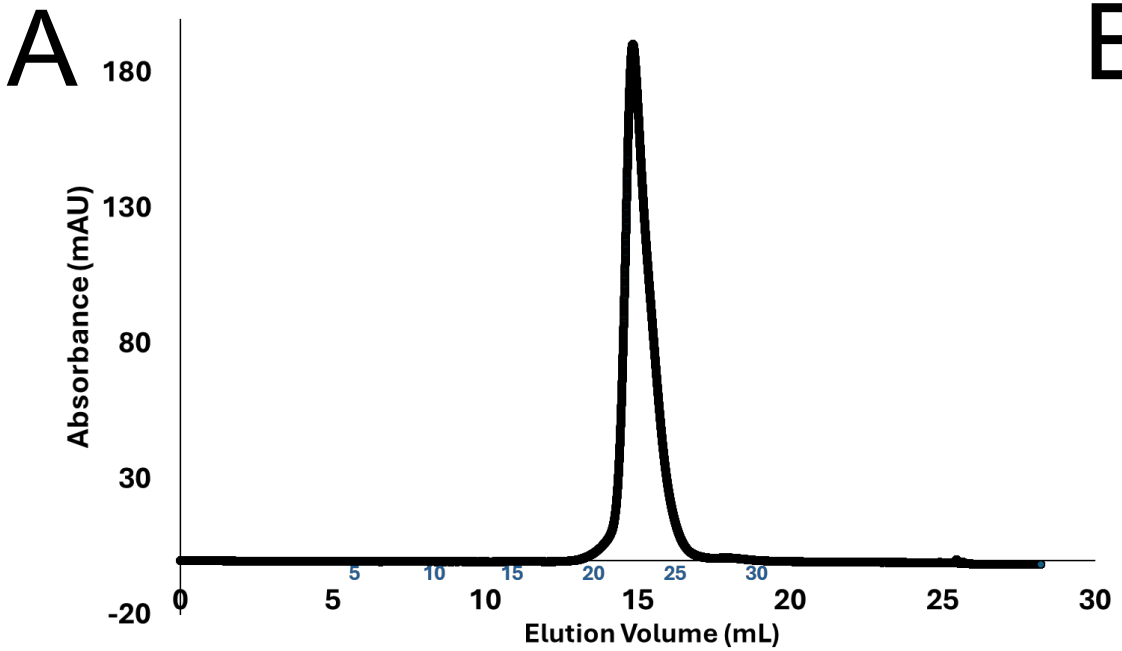


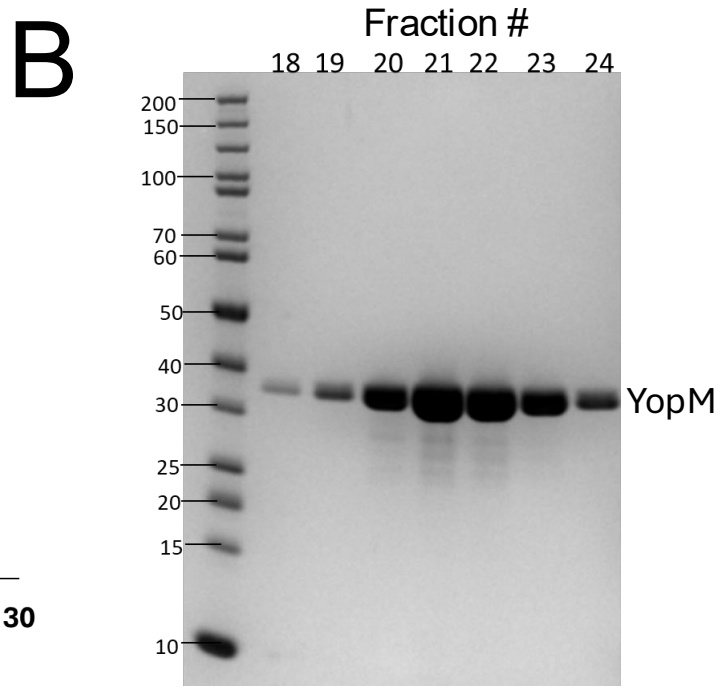


**Fig. S11. Characterization of YopM$^{\Delta N \Delta C}$ Ala2 and the YopM$^{\Delta N \Delta C}$ Ala2-hPYD interaction by SEC.** YopM$^{\Delta N \Delta C}$ at 4mg/mL (**A,B**) or a 1:1 molar mixture of YopM $^{\Delta N \Delta C}$ and hPYD at 2.3mg/mL (**C,D**) were analyzed by SEC on a Superdex 200 10/300 column at 0.75mL/min. Samples were analyzed in 20mM HEPES, 150mM NaCl and 1mM TCEP pH 7.4 buffer. **A,C.** SEC chromatograms. **B,D**. Fractions of the peak elutions were analyzed by SDS-PAGE and blue protein staining.

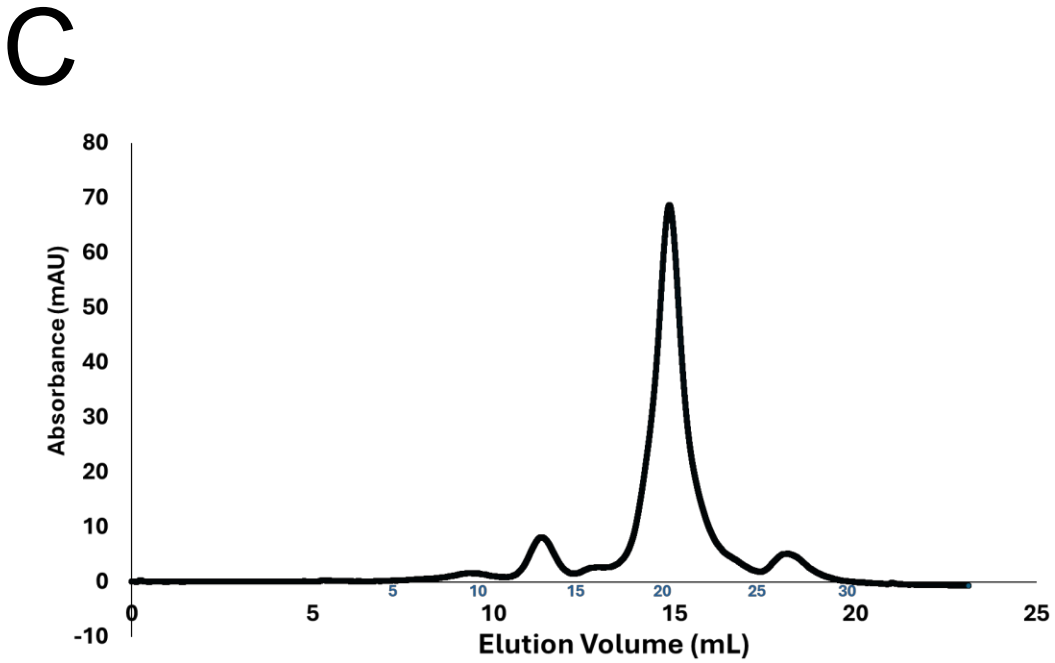


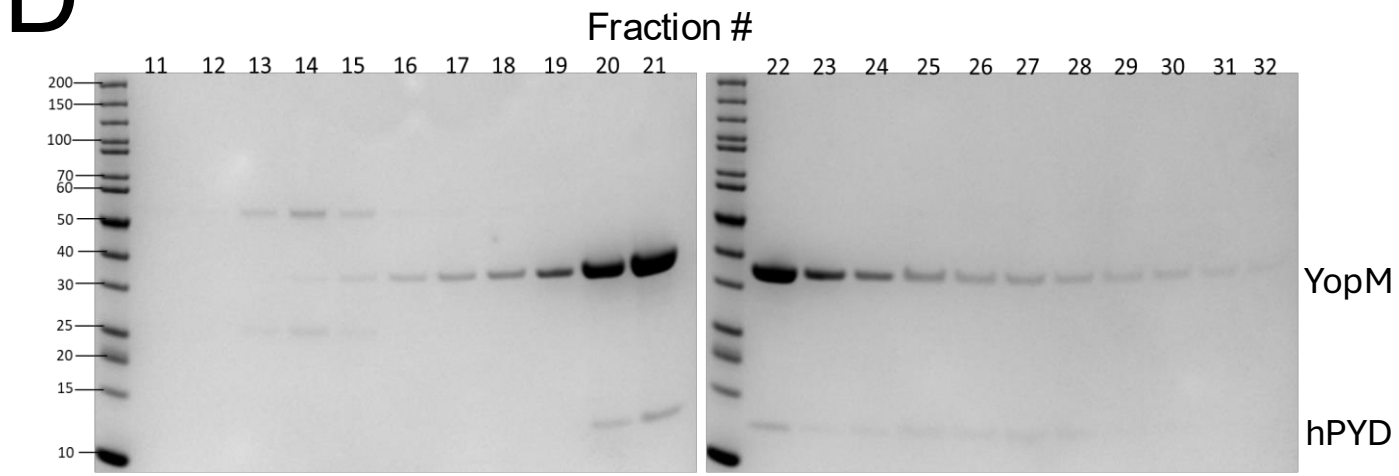

```
YopM KIM    1   M F I N P R N V S N T F L Q E P L R H S S N L T E M P V E A E N V K S K T E Y Y N A W S E W E R N A P P G N G E Q R E M   60
YopM PestA  1   M F I N P R N V S N T F L Q E P L R H S S N L T E M P V E A E N V K S K T E Y Y N A W S E W E R N A P P G N G E Q R E M   60
                                10                  20                  30                  40                  50                  60

                                70                  80                  90                  100                 110                 120
YopM KIM    61  A V S R L R D C L D R Q A H E L E L N N L G L S S L P E L P P H L E S L V A S C N S L T E L P E L P Q S L K S L L V D N   120
YopM PestA  61  A V S R L R D C L D R Q A H E L E L N N L G L S S L P E L P P H L E S L V A S C N S L T E L P E L P Q S L K S L L V D N   120
                                70                  80                  90                  100                 110                 120

                                130                 140                 150                 160                 170                 180
YopM KIM    121 N N L K A L S D L P P L L E Y L G V S N N Q L E K L P E L Q N S S F L K I I D V D N N S L K K L P D L P P S L E F I A A   180
YopM PestA  121 N N L K A L S D L P P L L E Y L G V S N N Q L E K L P E L Q N S S F L K I I D V D N N S L K K L P D L P P S L E F I A A   180
                                130                 140                 150                 160                 170                 180

                                190                 200                 210                 220                 230                 240
YopM KIM    181 G N N Q L E E L P E L Q N L P F L T A I Y A D N N S L K K L P D L P L S L E S I V A G N N I L E E L P E L Q N L P F L T   240
YopM PestA  181 G N N Q - - - - - - - - - - - - - - - - - - - - - - - - - - - - - - - - - - - - - - - - - - - - - - - - - - - L E E L P E L Q N L P F L T   198
                                                                                                                    190

                                250                 260                 270                 280                 290                 300
YopM KIM    241 T I Y A D N N L L K T L P D L P P S L E A L N V R D N Y L T D L P E L P Q S L T F L D V S E N I F S G L S E L P P N L Y   300
YopM PestA  199 T I Y A D N N L L K T L P D L P P S L E A L N V R D N Y L T D L P E L P Q S L T F L D V S E N I F S G L S E L P P N L Y   258
                200                 210                 220                 230                 240                 250

                                310                 320                 330                 340                 350                 360
YopM KIM    301 Y L N A S S N E I R S L C D L P P S L E E L N V S N N K L I E L P A L P P R L E R L I A S F N H L A E V P E L P Q N L K   360
YopM PestA  259 Y L N A S S N E I R S L C D L P P S L E E L N V S N N K L I E L P A L P P R L E R L I A S F N H L A E V P E L P Q N L K   318
                260                 270                 280                 290                 300                 310

                                370                 380                 390                 400
YopM KIM    361 Q L H V E Y N P L R E F P D I P E S V E D L R M N S E R V V D P Y E F A H E T T D K L E D D V F E   409
YopM PestA  319 Q L H V E Y N P L R E F P D I P E S V E D L R M N S E R V V D P Y E F A H E T T D K L E D D V F E   367
                320                 330                 340                 350                 360
```

**Fig. S12. Sequence alignment of YopM$^{KIM}$ and YopM$^{PestA}$** . Full-length sequences of the two proteins were aligned in Snapgene using ClustalW. Highlighted in red boxes are the residues changed in Ala2. In bold are the residues in YopM$^{KIM}$ which are missing in YopM$^{PestA}$.

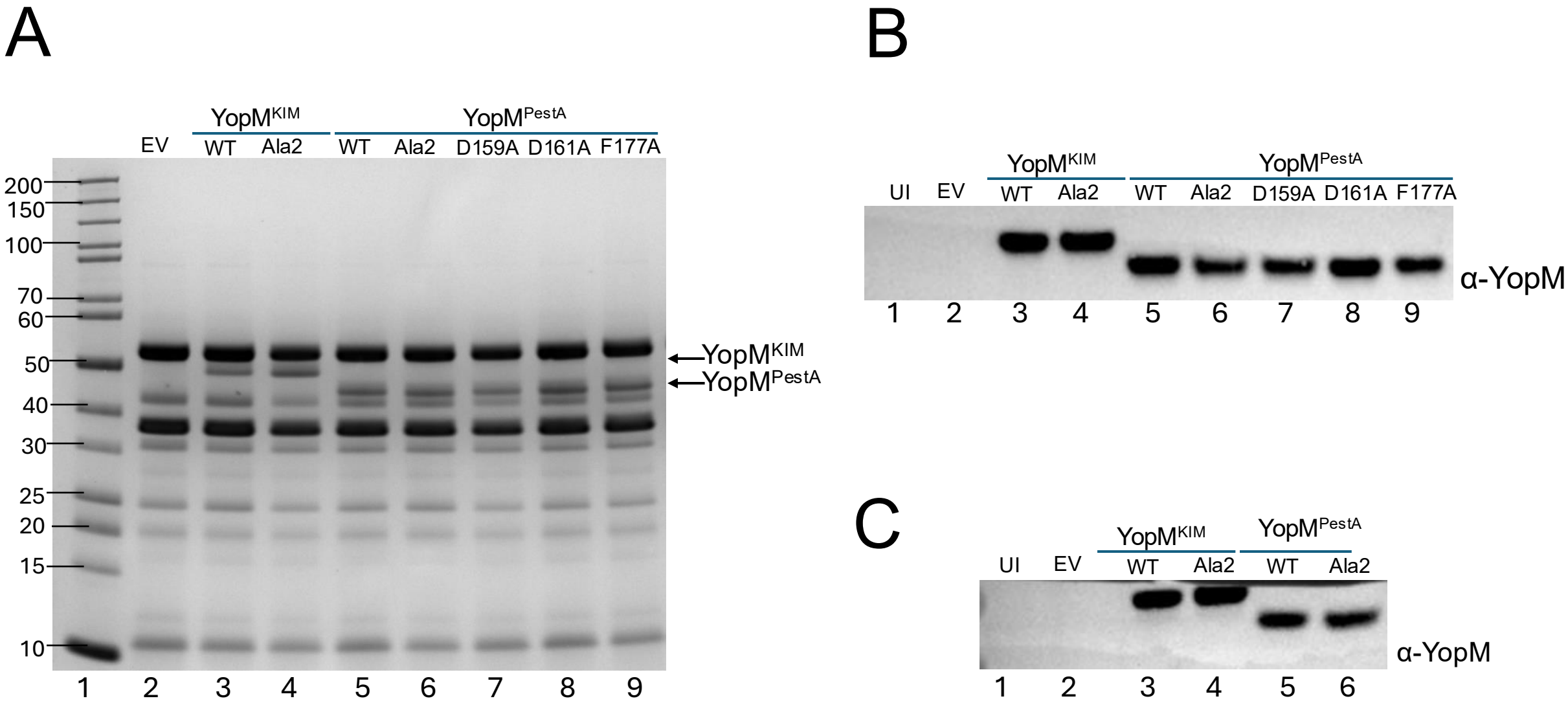


**Fig. S13. Analysis of YopM variant secretion and translocation. A)** *Y. pseudotuberculosis yopJ$^{C172A}$ΔyopM* strains complemented with empty vector (EV) or expressing the indicated YopM isoform or variant were grown under T3SS-inducing conditions and secreted Yops were collected and analyzed by SDS-PAGE and blue protein staining. THP-1 cells (**B**) or BMDMs (**C**) were left uninfected (UI) or infected with *Y. pseudotuberculosis yopJ$^{C172A}$ΔyopM* strains complemented with empty vector (EV) or expressing the indicated YopM isoform or variant. THP-1 infections were peras in Figs. 4C and 4D. BMDM infections were at MOI 30 for 90 min. Cell lysates were subjected to Immunoblotting with α-YopM.

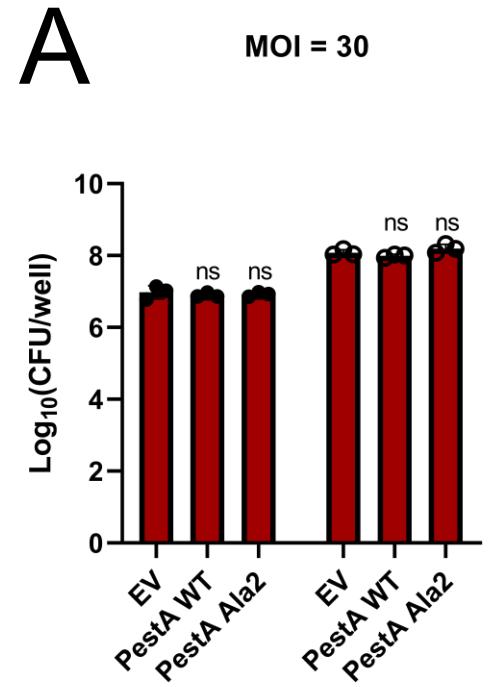


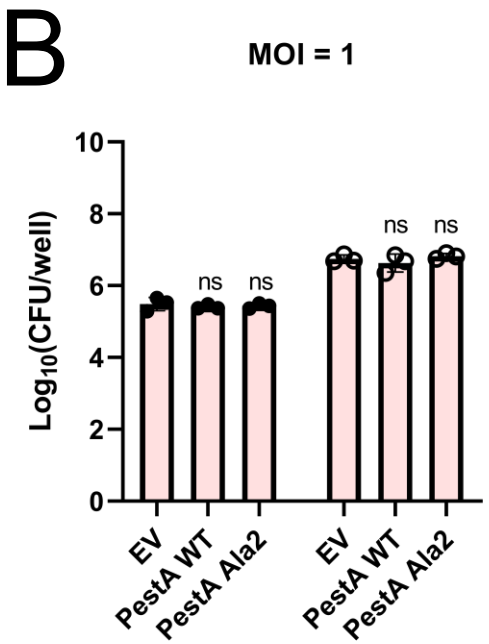


**Fig. S14. CFU recovery post-infection.** THP-1 cells were infected with the indicated strains of *Y. pseudotuberculosis* at an MOI=30 (**A**) or MOI=1 (**B**) for 4 h. Samples of bacteria inoculated into each well at t=0 h (closed circles) were serially diluted and plated for CFU quantification. Total bacterial-monocyte co-cultures were solubilized in 0.1% NP-40 detergent (t=4 h) followed by serial dilutions and plating to determine CFU recovery post-infection (open circles). Bars represent averages of 3 biological replicates. Error bars represent standard deviation. Significance was determined by one-way ANOVA and Tukey's *post hoc* test. Comparisons of each group to EV are shown; ns, not significant.

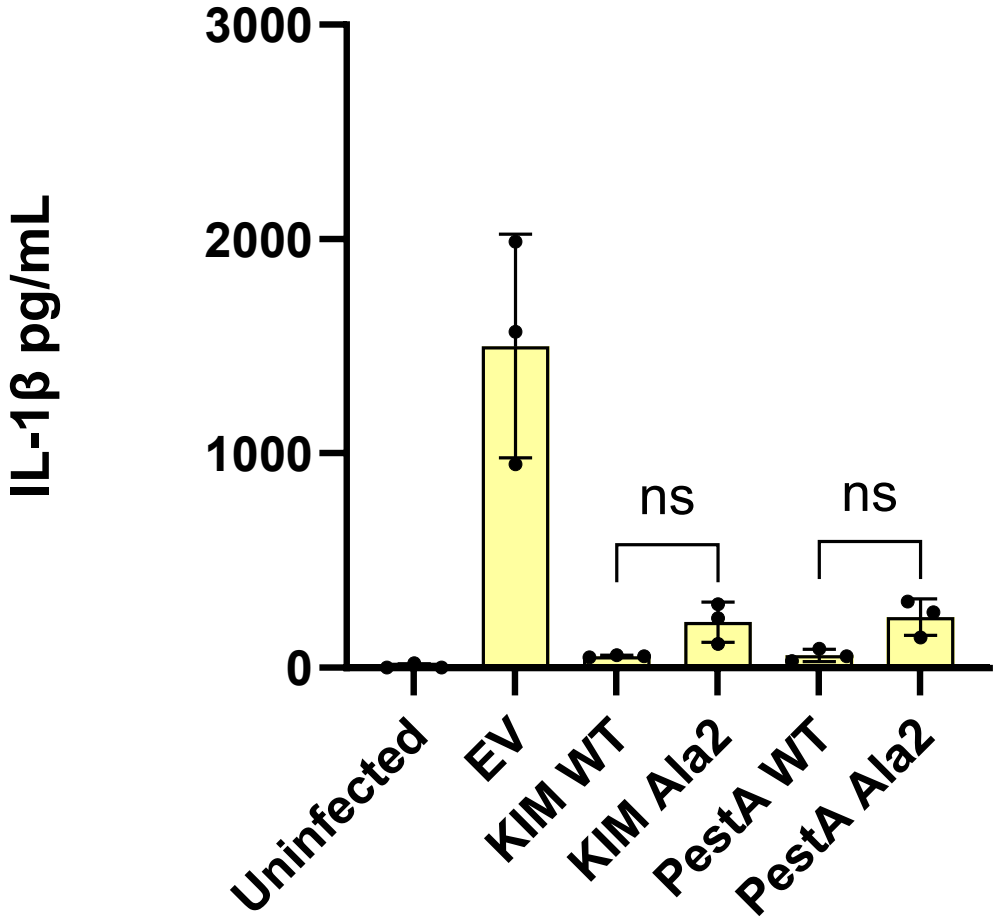


**Fig. S15. Analysis of YopM variants by BMDM infection assay.** LPS-primed BMDMs were left uninfected (UI) or infected with *Y. pseudotuberculosis yopJ*$^{C172A}$*ΔyopM* strains complemented with empty vector (EV) or expressing the indicated YopM isoform or variant. ELISA was used to measure releasedIL-1β. Results are averages and standard deviations with data pooled from at 3 independent experiments. Significance determined by one-way ANOVA and Tukey's post hoc test comparing WT YopM isoforms to their Ala2 variants as shown by brackets. ns, not significant.

A

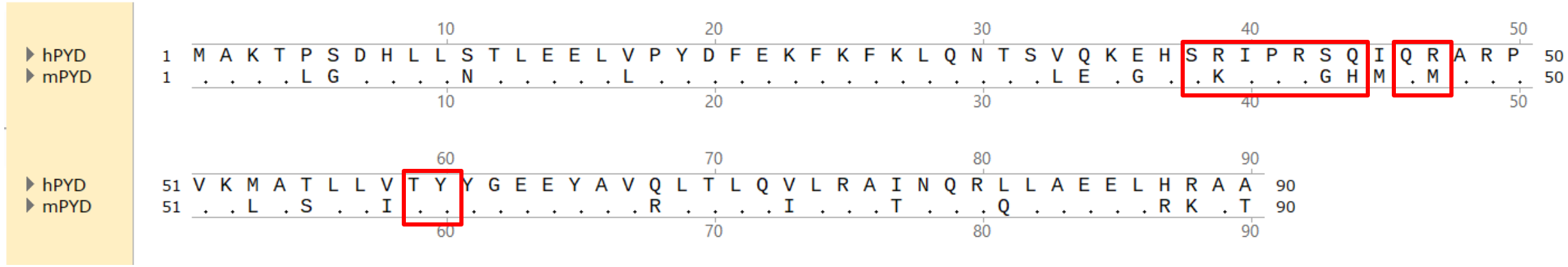


B

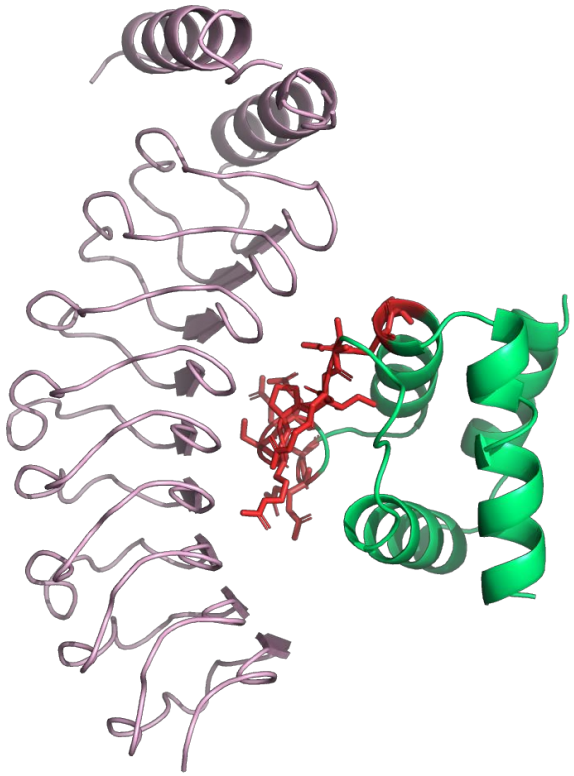

**Fig. S16. Sequence alignment of hPYD and mPYD and structure of the complex highlighting key contact residues in hPYD.** **A)** Sequences of hPYD and mPYD were aligned in Snapgene using ClustalW. Dots indicate identical residues at each position. Highlighted in red boxes are residues on hPYD participating in key interactions with YopM. **B)** YopM-hPYD* complex highlighting residues on hPYD as sticks in red that participate in key interactions with YopM.